Plasma DBD Electrodes

For a Seed Disinfection Fluidized Bed Reactor

Coen Buitink & Jeroen Lohman

July 13, 2024

TU Delft

Plasma DBD Electrodes

For a Seed Disinfection Fluidized Bed Reactor

by

Coen Buitink & Jeroen Lohman

to obtain the degree of Bachelor of Science
at the Delft University of Technology,
to be defended on Tuesday June 25, 2024 at 15:30 PM.

Students:	Coen Buitink	
	Jeroen Lohman	
Project duration:	April 22, 2024 – June 28, 2024	
Thesis committee:	Prof. dr. ir. J. van Turnhout,	TU Delft, supervisor & jury chair
	Dr. ing. H. van Zeijl,	TU Delft, supervisor
	M.D. L. Wymenga,	TU Delft, supervisor
	Dr. ir. A. van Genderen,	TU Delft, neutral assessor
Faculty:	Faculty of Electrical Engineering, Mathematics and Computer Science, Delft	

An electronic version of this thesis is available at http://repository.tudelft.nl/.

TU Delft

Abstract

As a novel alternative for conventional seed disinfection methods, a new design has been proposed in this report using a surface dielectric barrier discharge (SDBD) fractal electrode. The discharge mechanism for this electrode is a diffuse microdischarge under AC or short-pulsed DC mode operation. In this way, cold plasma could be generated that is applicable for seed disinfection. Furthermore, the electrodes were designed to be part of a proof of concept fluidized bed reactor with a reactor size of $10 \times 20 \times 20\ [cm]$ for disinfecting cabbage seeds with a diameter of $2\ mm$. Because of this application, the efficacy of seed decontamination using plasma with its generated reactive agents was discussed. The used gas mixture in which the electrodes created plasma was ambient air without increased humidity. This means that the main reactive agents for sterilisation are reactive oxygen species (RON) like ozone (O_3) and reactive nitrogen species (RNS). The electrical and physical parameters required to make cold-plasma were investigated to come up with a proper design for the electrode. From this theoretical analysis, five different initial designs emerged. The analysed designs include a wire-to-wire, wire-to-sheet, multi-hollow DBD, fractal SDBD and a coplanar DBD fractal electrode. All electrode designs were made based on the state-of-the-art dielectric barrier discharge principle. Moreover, in the design consideration, different materials for the conductor and dielectric were discussed, mainly based on electrical properties, plasma generation and manufacturing possibilities were considered. Based on previously set trade of requirements, together with the results of measured power and turn on voltage of the plasma electrodes, the best designs tested design for seed disinfection are the double-sided 5^{th} order Hilbert fractal with a $1.6\ mm$ barrier and the single-sided 5^{th} order Hilbert fractal with a $0.8\ mm$ barrier.

Preface

Coen Buitink & Jeroen Lohman
Delft, June 2024

This work is part of a group project in the Electrical Engineering bachelor graduation project. The project was proposed by global leading seed manufacturer Bejo Zaden B.V. from Warmenhuizen. Bejo Zaden currently treat many of their seeds using the hot water bath method. However due to complications in performance and loss of product, they proposed this project to let us students investigate the novel technique of cold plasma for seed disinfection. To make a proof of concept design that could be applied for industry, a fluidized bed reactor was suggested by Bejo Zaden. The student group divided the tasks for this proof of concept into three categories: the fluidized bed and sensors [1], high voltage power supply [2] and the plasma electrode design, of which the latter group this report is dedicated to.

For this project, we want to thank our daily supervisor Luutzen Wymenga, who was already working on novel designs for cold plasma electrodes. Thanks to him, we eventually settled with the most effective design, namely a space-filling Hilbert curve electrode. Besides, we want to thank him greatly for the time he made available for us to test in the High Voltage lab of our faculty. Without his expertise and testing setup, testing the electrodes in the short project would not have been possible. Next, we would like to thank professor Jan van Turnhout for his motivating spirit and giving us constant new ideas for improvements. Additionally, our supervisor Henk van Zeijl helped us think about the implications of our design choices, which were useful to deliver a proof of concept design for Bejo Zaden. Besides our supervisors, we want to acknowledge our fellow students from mechanical engineering Toby Schoppink, Ymke Vredenbregt and Lodewijk Zoetmulder, who gave us useful information about their findings of plasma seed disinfection using electrodes. Finally, our praise goes to our contact at Bejo Zaden Yvette Bakker. Her feedback during the presentation sessions throughout the project gave better insight in how seed disinfection works and on what disinfection parameters should be focused.

Now that we are finished with the project, we as a subgroup are grateful how we worked together and pushed through on long lab days in Tellegen hall or the High Voltage lab with our fellow teammates Zakaria Hayaty, Paul Lee, Thomas Ritmeester and Berke Salar. In particular, we would like to thanks Thomas for his extra effort to, alongside his own subgroup tasks, make our electrode designs possible with his CNC machine and CAD programme skills. Otherwise, fast and affordable prototyping of the different fractal designs would not have been possible.

Contents

1 Introduction

1.1. Project Objective

Since the time humans started farming ages ago, the aim of farming has evolved to obtain the best yield from the planted seeds. Planting in nutrient soil, adequate irrigation, and sunlight were all known factors to obtain successful crops and fruits. However, due to the growth of the agricultural sector, the spread of plant diseases has grown simultaneously. Not surprisingly, the seed manufacturing industry has become an advanced field that aims to produce the most vital, best preservable, and fast germinating seeds. It provides a large market of farmers and cultivators and essential serves the quality and quantity of our society's crop and fruit supplies. Well-known methods as selective seed breeding are used to obtain the best possible seeds for the market. Additionally, to reduce the seeds that are infected with diseases, seeds are currently processed with disinfection methods. However, these approaches are often energy-inefficient and cause chemical waste. To improve this, seed manufacturers desire a new seed disinfection process that maintains the vitality of seeds while simultaneously being eco-friendly, cost effective, and sufficiently disinfecting. Cold plasma, a recent emerging field of research could be an solution for these problems. The objective of the full project group is to design a prototype disinfection machine using cold plasma. For the subgroup concerning this report, the objective will be to design electrodes of the fluidized bed reactor that produces reactive species from cold plasma that inactivate microorganisms on seeds.

The project proposer for this project Bejo has requested a new method of seed disinfection that could be scaled up and be more energy efficient than their current method of hot water baths. Furthermore, the scope of this project is to design electrodes that fit in a fluidized bed reactor and produce disinfectants efficiently in the given space of the reactor. The created reactive species should come in close contact with the electrodes where the cold plasma is generated. The goal of this project to design an disinfection system that works for cabbage seeds of $2\ mm$ in diameter. Parameters that will be tested are the concentration values for ozone and ions. Several designs will be analysed that aim to obtain a large cold plasma production area within a voltage range of $10\ kV$. The designs considered are mainly concerned with the integration in the fluidized bed, such that the circulation of disinfectants is optimal for the seeds. This means that different designs will be analysed based on their plasma production and air obstruction in the fluidized bed.

1.2. State-of-the-Art Analysis

In the current seed processing system, seeds are treated in hot water baths. The use of a hot water bath has as primary effect to eradicate seed diseased which are caused by phytopathogenic bacteria (bacteria that are parasitic for plants). This method works for a variety of seeds, though it is more effective for one type than another. Furthermore, the difficulty with the current hot water treatment method is that the accuracy of temperature and timing is crucial. That is, cold water could cause unsprouted seeds to turn into an incomplete dormancy state. However, too hot water would kill the seeds. This limits the available seeds that could be treated to only seeds with a high vitality [3]. Additionally, for older seeds (more than one year old) or seeds that were grown in a stressful environment, hot water

treatment can decrease the germination rates [4]. Typical treatment times for effective disinfection from bacteria and fungi range from 10 to 30 minutes in a hot water bath of about $50°C$ [5].

New innovative methods to disinfect seeds that are non-thermal have been explored in recent years like pulsed ultraviolet-light and ozone processing. Specifically UV-c light is effective for inactivation of microorganisms. The type of ultraviolet light causes mutations in the nucleic acids of bacteria and viruses, resulting in a reduction in the microbial population curve. To successfully disinfect seeds from microorganisms using UV-c, the photons of the light need to directly strike the seed's surface [6, p.5]. For this reason, the UV-c sterilisation method affects only the surface of the seeds, which is considered sufficient to maintain the hygiene of the seed [7]. However, it does pose limitations in batch processing of seeds due to light penetration issues or shadowing effects. The other method, ozone processing, has gained increasing interest, as consumers regard it as a "greener" food additive and an environmentally friendly technology [6, p.5]. Ozone has antimicrobial properties and can more easily come in contact with the seeds' surface by diffusion contrary to direct UV-light exposure.

As can be derived from these disinfection solutions, the industry and academic research is pursuing for new seed disinfection solutions that are more sustainable whilst being not being invasive on the seed's health. Subsequently, non-thermal plasma (NTP) or cold plasma treatment solutions became an interesting area of research since it could possibly deal with all the aforementioned criteria and shortcomings of current seed disinfection methods.
Plasma is often considered as the fourth state of matter with the highest energy state compared to the energy hierarchy composed of the well-known states solid, liquid and gas, as can be seen in Figure 1.1. Plasma can be seen as an ionized state of a gas that can be created by any source of energy. Moreover, plasma is comprised of several excited atomic, molecular and reactive species, such as electrons, positive and negative ions and even quanta of electromagnetic radiation like UV photons and visible light. Most importantly, the majority of the chemical species generated with a plasma are characterised as very effective for microbial disinfection [6, p. 8].

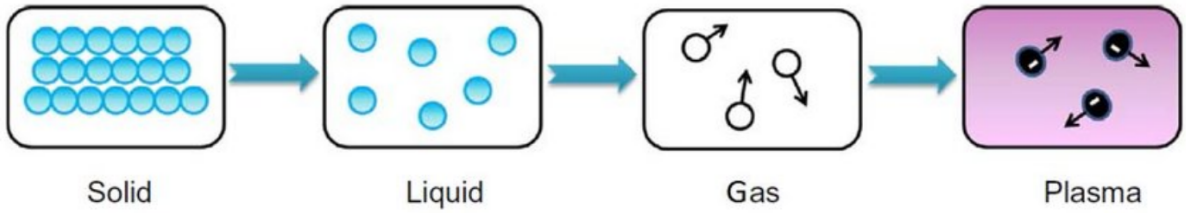

Figure 1.1: Hierarchical representation of the four states of matter, adopted from [6]

Returning to non-thermal plasma, it is characterised as plasma that is below $60°C$ and obtained by strong electric fields which causes discharges in gases. Moreover, the generated ions and reactive species are dependent on the used gas. For instance, air generated plasmas contain reactive oxygen species (ROS) like hydrogen peroxide (H_2O_2), hydroxyl radicals ($OH^{\bullet}$), ozone (O_3) and reactive nitrogen species (RNS) such as nitric oxide ($NO^{\bullet}$) and nitrogen dioxide radical ($NO_2^{\bullet}$) [8]. Furthermore, NTP can be created at atmospheric pressure or reduced pressures and requires less power than thermal plasmas. To actually generate the plasma at atmospheric pressure the following discharge principles could be used: corona discharge, dielectric barrier discharge (DBD), radio-frequency plasma and gliding arc discharge.

From the latter, dielectric barrier discharge is often used for plasma sterilisation purposes, as it has many implementation options. Using this variation of plasma generation, seeds can be treated by coming into direct contact or from a distance away from the plasma. Additionally, seeds could be soaked in water before a plasma treatment, providing additional reactive species from the molecules in water. This form is called plasma activated water (PAW), but could also be performed with other plasma activated media (PAM) that are gases or liquids [8]. Resuming with dielectric barrier discharge, a DBD can be created from two electrodes from which at least one of the two electrodes is isolated from the gas using a dielectric. Furthermore, the distance of the discharge gap and gas pressure be-

tween the electrodes dictate the required voltage to obtain a discharge. Typical values range between $0.1 - 10\ mm$ and $1 - 100\ kV$ respectively [9]. Some conventional planar configurations for DBDs is displayed in Figure 1.2.

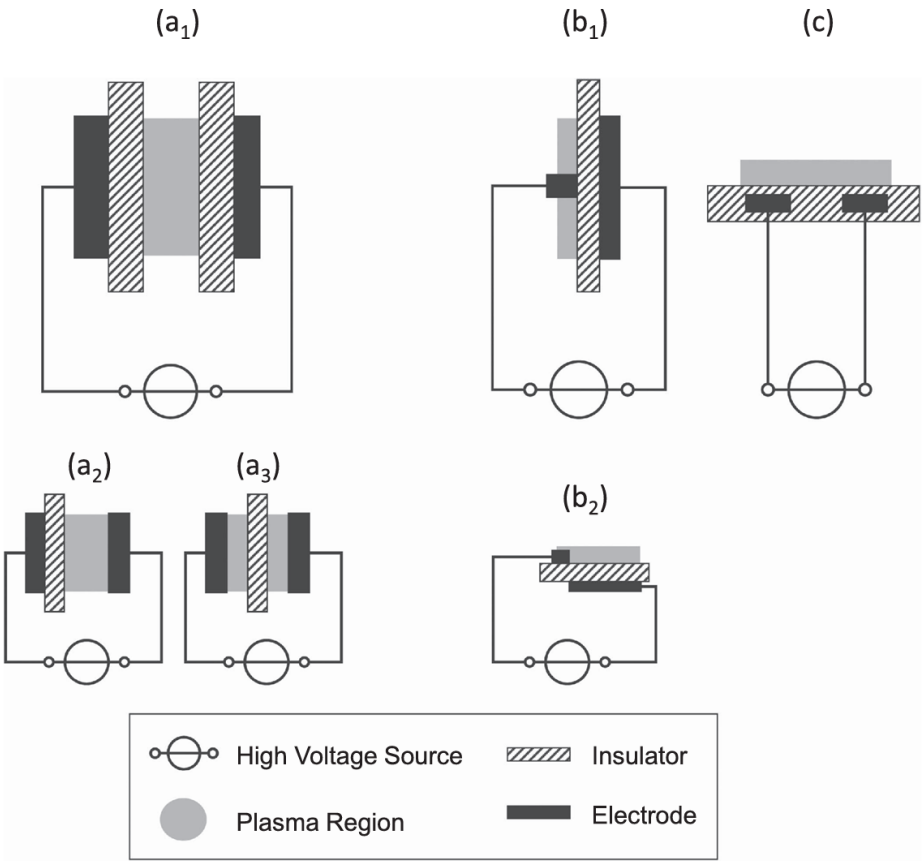

Figure 1.2: Conventional planar-DBD configurations. (a) volume DBD (1-symmetric, 2-asymmetric, 3-floated dielectric); (b) surface DBD (1-symmetric, 2-asymmetric 'actuator' design); (c) coplanar discharge, adopted from [9]

What remains to be investigated is the most effective configuration of DBD electrodes for a fluidized bed reactor. The sizing of the fluidized bed itself will already limit some of the available configurations. Furthermore, the optimal geometrical, material and electrical parameters have to be determined for the electrodes. That is because these parameters will mainly determine the electric field formation that causes the discharge in the gas of the fluidized bed reactor

1.3. Thesis Outline

This thesis will be structured in the following parts. In the first succeeding chapter, the programme of project requirements will will be listed based on the needs of the user of the fluidized bed. These user needs are stated based on user stories, after which tasks are categorised as mandatory and trade-off requirements. After the requirements are set, the more specific characteristics of cold plasma will be explained. In brief, the topics concern the physics, types of discharges and electrical background as well as the effectiveness of reactive species. Next, the design principles concerning the material and geometrical effects on the electrodes are discussed. Moreover, an explanation will be given on how fabrication and electrical safety are factored into the design. In the following chapter, the measurement techniques and modelling of the electrode designs are specified. Finally, the measurement results will be presented in terms of plasma formation photos and Lissajous figures for power dissipation, as well as the discussion of the different design results and the conclusion for the final electrode design.

2

Programme of Requirements

Before starting the design process, a programme of requirements (PoR) has been established as a guideline for the plasma electrode design. It specifies the requirements of the final product according to the needs of the end-user of the plasma fluidized bed reactor. The target user is a seed producer and their desires will be defined based on user stories (US). From there, the user stories are categorised in Mandatory Requirements (MR) and Trade-off Requirements (ToR) for the electrode design. Furthermore, the PoR is specifically constructed for the plasma electrodes, although some customer needs could also partially concern other parts of the plasma fluidized bed system. Finally, it should be noted that since this report describes a product that will be a proof-of-concept, the PoR will have to be updated when the product is further developed for commercial use.

2.1. User Stories

US.1 As a seed producer, I want to use a cold-plasma disinfection machine that can effectively disinfect seeds in a short time frame so that the disinfection process can be accelerated.

US.2 As a seed producer, I want to have a reactor design that is modular such that components can be taken out easily for maintenance or replacement.

US.3 As a seed producer, I want to have a disinfection process that does not harm the germination of the treated seeds so that I do not have a loss of product.

US.4 As a seed producer, I want that the system is safe to use when in operation such that operators are not exposed to potential risk.

US.5 As a seed producer, I want to have a design that is scalable so that I can later expand to larger seed disinfection batch cycles.

US.6 As a seed producer, I do not want to have to replace the plasma generating components after every disinfection process so that I can have a continuous process.

US.7 As a seed producer, I want to have plasma electrodes that can be easily manufactured, so that the repair cost and repair time are low.

US.8 As a seed producer, I want to have a system that does not have to be cleaned often due to dirt or debris, so that it requires less maintenance.

2.2. Mandatory Requirements

MR.1 Plasma electrodes must fit in a fluidized bed reactor of $10 \times 20 \times 20$ $[cm]$;

MR.2 Distances between electrodes, including dielectric thickness must allow plasma-formation below 10 kV and draw a current not higher than in the order of mA;

MR.3 The created plasma must output reactive species and ions.

MR.3.1 From these reactive species, they must contain reactive oxygen species (ROS) like ozone.

MR.3.2 The generated reactive species by the plasma must not be harmful for the seeds such that it reduces germination.

MR.4 The plasma electrodes shall not break due to sparks when in a disinfection cycle;

MR.5 Plasma must be formed in air under atmospheric pressure;

MR.6 The temperature of the electrodes must not exceed 50°C;

MR.7 The electrodes must allow plasma formation with a DC pulsed and AC power supply.

MR.8 The dielectric elements of the plasma electrodes must have a dielectric strength greater than the final applied electric field;

MR.9 When placed inside the fluidized bed reactor, the electrodes must be electrically isolated from the outside shell of the system.

MR.10 The connectors of the electrodes must be able to easily connect to the power supply unit using off the shelf components.

MR.11 The disinfecting performance of the generated plasma must be such that within 10 minutes, the microbial activity on the cabbage seeds has been reduced by at least 80%.

2.3. Trade-off Requirements

ToR.1 Preferably, the electrodes should not interfere with the seed fluidization in the fluidized bed;

ToR.2 The plasma electrodes should create the most possible regions of plasma per area;

ToR.3 The maintainers of the fluidized bed reactor should be able to replace individual electrode units for maintenance or replacement and thus require a modular design.

ToR.4 The electrodes should be able to withstand seed impact during the fluidization process;

ToR.5 Preferably, possible dirt and debris build-up on the electrodes during a disinfection cycle should not break or stop the plasma formation;

ToR.6 The electrode connections should have clear labels indicating the ground and live connection points;

ToR.7 Preferably, the final design of electrodes should be able to be manufactured in bulk without the need of complex machinery.

ToR.8 The design of the electrode should be scalable for larger fluidized bed reactors.

3

Characteristics of Cold Plasma in DBD Systems

3.1. Physics and Characteristics of Cold Plasma

The main principle behind the creation of cold plasma is the breakdown process, which is the ionisation of a gas. The air consists of mostly neutral atoms and molecules; only a fraction are charged ions and free electrons. These charged particles originate from cosmic rays, causing a density in the order of $10^9 m^{-3}$ at sea level. In the event an electric field is present, these charges will accelerate towards their respective opposite polarity. However, the movement of ions and electrons does not go uninterrupted, which means that they will collide with other neutral molecules in the air. These collisions will transfer energy to the respective air molecules, of which the characteristic will differ between ions and electron collisions. Additionally, the exchange of energy depends on the ratio between the masses m_1 and m_2 that strike each other. Since electrons (m_1) generally weigh lighter than the collided neutral particle (m_2): $m_1/m_2 << 1$, only a small fraction of the available energy can be exchanged. In contrast to ions, the masses are in most cases almost equal: $m_1/m_2 \approx 1$, meaning almost all the energy will be transferred such that the ion stops moving after the collision. Consequently, using an applied electric field, the electrons will accelerate and carry the electrical energy into the creation of reactive radicals [10, p. 17]. Only the electrons will be heated inside the formed electric field and not the surrounding gas molecules. This nonequilibrium behaviour forms the basis for the most cold plasma applications. The difference in gas and electron temperature is commonly a ratio of 100, depending on the type of gas and pressure [10, p. 18].

3.1.1. Breakdown Mechanism

The level of electric field required to cause an ionisation effect is described by the breakdown voltage. The breakdown voltage for different type of gasses was found empirically by Paschen in the 19^{th} century. The formula from [10, p. 36] describes the breakdown curves is as follows:

$$V_B = \frac{A \cdot p \cdot d}{ln(B \cdot p \cdot d) - ln(C)} \tag{3.1}$$

Here, A, B and C are coefficients that depend on both the gas and the electrode material and would be empirically defined. The minimum voltage for a breakdown is formulated as Equation 3.2:

$$V_{B,min} = e^1 \cdot \frac{A \cdot C}{B} \tag{3.2}$$

When calculating for the voltage minimum, the corresponding pd value can be found as per Equation 3.3

$$(pd)_{min} = e^1 \cdot \frac{C}{B} \tag{3.3}$$

For the given curve presented in Figure 3.1, the minimum breakdown voltage is around $0.6\ Pa\ m$ in air. As it is required that the electrodes should work at atmospheric pressure ($101325\ Pa$), the distance for

achieving the minimum breakdown voltage would be very small:

$$d = \frac{0.6}{101325} \approx 6\,\mu m \tag{3.4}$$

The resulting distance from Equation 3.4 would be very difficult to realise on an electrode with great accuracy. Nonetheless, the applied voltage requirement is larger than the operating voltage for the V_B minimum, which hovers around $500\,V$. Provided that in Figure 3.1 at a breakdown voltage of $8\,kV$ the pd value is $100\,Pa\,m$, the electrode spacing would already become:

$$d = \frac{100}{101325} \approx 1\,mm$$

Thus, for an even larger voltage, which is possible given the $10\,kV$ requirement **MR.2**, the electrode spacing fabrication needs less accuracy to still be able to obtain a breakdown. Furthermore, the larger voltage enables to create a plasma at atmospheric pressure, thereby satisfying the requirement **MR.5**.

The shape of the Paschen curve is governed by the electron impact ionisation in the gas phase and the secondary emission from electrodes. The secondary emission occurs due to ions striking the cathode electrode surface that has a certain probability of releasing an electron. This probability is often denoted by γ and depends on the chosen electrode material. Typically, the value is small, that is, $\gamma \lesssim 0.01$.

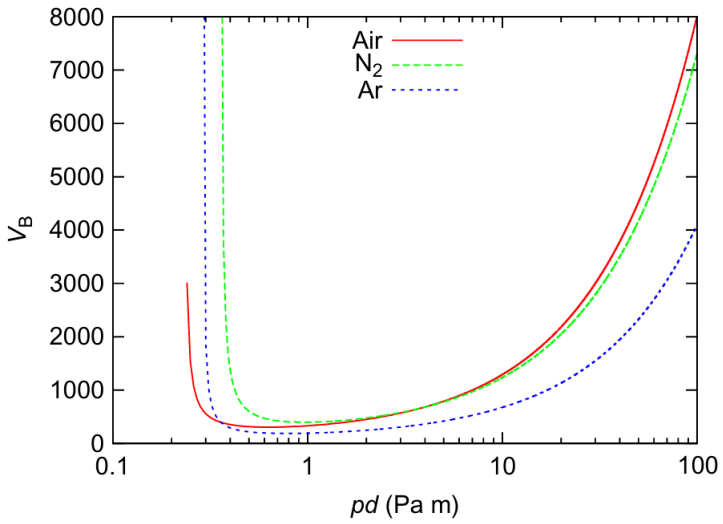

Figure 3.1: Paschen curves for air, nitrogen and argon from [10, p. 36]

3.2. Types of Discharges

3.2.1. Discharge Phenomena

The two processes together from the previous section, the gas phase ionisation and secondary emission from the cathode, are known as the Townsend breakdown process. Townsend breakdown can only occur if an net increase in charged particles is created. Thus $1/\gamma$ ions should be produced by the electron impact ionisation due to the electric field between the cathode and anode. Furthermore, it is assumed that the charges caused during the ionisation in the Townsend breakdown process do not alter the electric field. The primary electron that caused the first ionisation expands into a cloud of electrons. The motion of the electrons inside the spherical cloud is a combination of diffusion and the applied electric field. As a consequence, due to the drift the expanding electron cloud will move towards the anode. Indeed, the heavier ions created during the Townsend process will drift much slower towards the cathode. Under these circumstances a space charge region formed due to the separation of charges: the negative electrons inside the faster moving electron cloud and the slower ions that are left behind and form a positive region. Subsequently, the separated charges will create an opposing

electric field. In the case that this opposed electric field becomes greater than the applied electric field, the Townsend mechanism ceases to apply. More specifically, according to Turner [10, p. 37], the condition for the existence of the Townsend breakdown processes is described by the Raether-Meek criterion. The Raether-Meek criterion is a function of the Townsend ionisation coefficient α and the distance between electrodes: $\alpha(E/N)d \approx 20$

When above this threshold, the electric field is a function of both the applied electric field and the distribution of charges in the gap. The α parameter itself depends mainly on the ratio between the electric field E and the gas density N, known as the reduced electric field: E/N. In another article about air plasma sources [11], the E/N is a ratio that can be used to quantify the electron energy, which is important for the chemical reactions created inside the plasma.

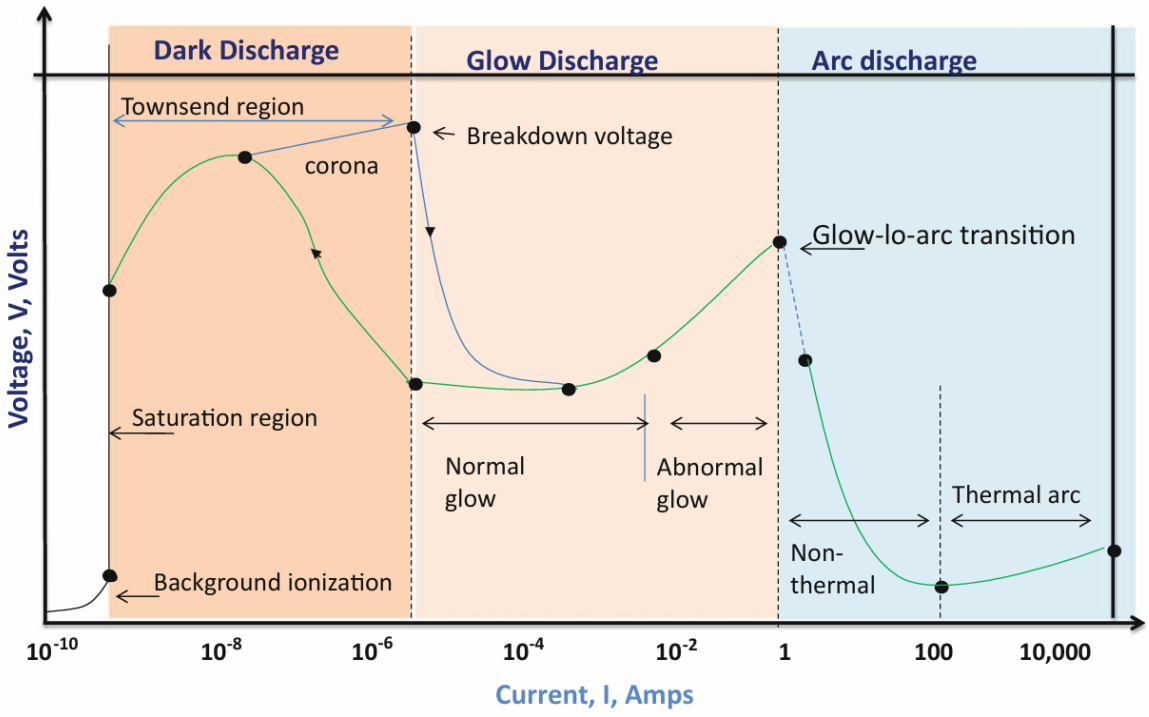

Figure 3.2: Current-Voltage characteristics of gas discharges showing the different discharge regions, adopted from [12, p. 701]

Besides of the chemical reaction, the spatial structure of the plasma is different once the Raether-Meek criterion is reached. Namely, Townsend breakdown produces diffuse plasma, whereas the Raether-Meek mechanism causes a so-called streamer plasma discharge. The visual differences between the two is that a streamer breakdown is a small arc or filamentary discharge over the region, meaning that only a small portion of the available area is filled with plasma. This is in most cases undesirable, as a higher currents could quickly lead to thermal discharges, as can be seen in Figure 3.2. Moreover, the majority of the energy consumed is consumed by gas heating instead of initiating the creation of reactive radicals. To overcome the heating problem is by limiting the this discharge current using a pulsed or alternating power supply or a dielectric barrier [12, p. 702]. In DBD applications, it is common to use both methods to reduce the streamer formation. The insulating effect of the dielectric causes charges to be accumulated and form an opposing electric field, which leads to the self-extinguishing behaviour of streamers in DBD. The collapse of the streamer happens only a few nanoseconds after breakdown. Thereby contributing to the low gas heating. During the rising external voltage, at some points the Raether-Meek criterion will be reached locally. This causes many smaller streamer breakdowns, also called microdischarges. As long as the voltage keeps rising, new microdischarge locations will be formed due to the presence of residual charges on the dielectric layer. These residual charges have reduced the electric field at the specific locations where microdischarges already

have occurred in the previous cycles. Moreover, these residual charges initiate a memory effect, as new microdischarges will be formed at the same locations. Above all, the following phenomenon could be observed according to U. Kogelschatz: high voltage low frequency operations tend to spread the microdischarges, while low voltage high frequency operation tends to reignite the old microdischarge channels every half period [13]. So, the effect that is observed in plasmas created by DBDs, is not an diffuse discharge but rather a collection of multiple microdischarges along the electrode edge and are repeated every second according to the set frequency of the power source [9]. In order to obtain real diffuse 'glow' discharges, that is the middle region displayed Figure 3.2, lower pressures are required in the $0.1 - 100\ Pa$ range [14, p. 13].

Now, it is clear that dielectric barrier discharges are fundamentally the same as conventional streamer breakdowns with a similar external electric field distribution. Though, the presence of the dielectric barrier alters the gap electric field strength. Since there are effectively two regions over which the discharge will take place, the gap field strength in air will be higher than the average field strength. This is because the dielectric constant of the dielectric layer is higher than the value of gap gas, in this case air. In general, a thicker insulating layer requires a higher applied voltage to cause breakdown. The electric field strength can be described with a continuity of flux density equation, adopted from [15]. Starting with the continuity Equation 3.5:

$$\frac{E_d}{E_g} = \frac{\epsilon_d}{\epsilon_g} \tag{3.5}$$

Together with the general formula for voltage related to electric field and distance through the gap and dielectric (l_d and l_g):

$$V = l_d \cdot E_d + l_g \cdot E_g \tag{3.6}$$

And solving for the respective electric fields in the different DBD regions, the electric field in the air gap (E_g) and in the dielectric (E_d) can be found by Equation 3.7:

$$\begin{aligned} E_d &= \frac{V \cdot \epsilon_g}{l_d \cdot \epsilon_g + l_g \cdot \epsilon_d} \\ E_g &= \frac{V \cdot \epsilon_d}{l_d \cdot \epsilon_g + l_g \cdot \epsilon_d} \end{aligned} \tag{3.7}$$

Using Equations 3.7, parameters such as thickness and dielectric constant could be optimised to obtain a plasma over air, which is typically $30\ kV/cm$ and a sufficient electric field over the dielectric that does not exceed the dielectric strength value. These parameters are important for the requirements **MR.4**, **MR.5** and **MR.8**.

3.2.2. AC Versus DC Pulsed Discharge

Since DBD can be generated from two type of sources, namely AC ad DC pulsed, the two will be briefly discussed by giving a top level overview their discharge characteristics. Later, the method for power calculation for both methods will be discussed more thoroughly. In addition, the two approaches have differences in the generation of reactive species, which will be discussed at the end of this chapter.

In many studies about dielectric barrier discharge, AC power supplies are commonly used to ignite a discharge over a dielectric barrier. However, DBD can operate in two power modes, namely AC and DC pulsed. As described in the previous Section 3.2.1, having an varying supply of current is important to create repeating filamentary discharge channels. Additionally, excitation causes a plasma to appear at the positive and negative applied voltage peak of one period. The plasma will become visible with AC if the breakdown voltage threshold is met and shows itself in very distinct bright spots along the electrode [16]. The frequency of the AC supply for the DBD can be a broad range from $50\ Hz$ to $1\ MHz$ [15]. The frequency is important for the power that will be deposited into a plasma for reactive species generation. The conventional method to measure the power of an AC excited discharge was discovered by Manley, also known as the Lissajous method [16]. The method uses a capacitor in series with the DBD electrode that is much larger than the device's capacitance. This capacitance is placed such that it accumulates the total charge of one AC half-cycle. The voltage of this capacitor is plotted against the discharge voltage to form the full Lissajous plot. In this way, the contributions of both the

displacement and discharge current can be evaluated.

Although AC supplied discharges were commonly used for many research papers over the years, nano to microsecond pulsed DC dielectric barrier discharges have gained increasing interest recently due to their distinct advantages over AC DBD. The nanosecond pulsed discharges can deliver a highly nonequilibrium state for the electrons, due to the fact that it enables higher voltage amplitudes to energise electrons within the nanosecond range. The duration of typical pulses is $100 - 500\ ns$, from which the rise time is in the order of $10 - 100\ ns$. Furthermore, the repetition frequency could be up to tens of kHz. As the duration of pulses is very short, the energy per pulse will be very low, providing a more safer method of high pulsed discharges over low frequency AC with voltage or conventional DC. It should be noted that configurations of electrodes does not have to be different from AC driven plasma electrodes. However, pulsed DC relies on state-of-the-art pulsed power discharges [15]. Pulsed power supplies are an extensive study area on its own. Therefore, only the effects of DC pulsed discharges will be of main interest in this report regarding the plasma electrode development. According to H. Jiang and T. Shao [17], ns surface dielectric barrier discharges (SDBD) at atmosphereic pressure essentially behave like filamentary discharges. The frequency mainly influenced the intensity of the plasma, while the voltage amplitude affected the width of the plasma region. This coincides with a study from N.D. Wilde et al. [18], who made a model describing the DBD discharge power according to its physical parameters, voltage and frequency. Here, it is described that the average plasma width ($\overline{x_p}$) is a function of a model fitted constant c_1, breakdown or ignition voltage V_{ign} and the applied peak-to-peak voltage (V_{pp}), as can be seen in Equation 3.8. Additionally, it was mentioned that the power of a discharge is proportional to the frequency $P \propto f$.

$$\overline{x_p} = c_1 \cdot \frac{V_{pp} - V_{ign}}{2} \tag{3.8}$$

Resuming with the advantages over AC discharge, DC pulsed offers a more diffuse discharge that is much more uniform than the irregular microdischarges from AC breakdown. Furthermore, the nanosecond pulses' discharge voltage and current exhibit bipolar pulse forms generated during the rise and fall time of the pulse. Due to the fast rise time, stronger discharge currents can be observed in single microdischarges. To give an illustration, conducted experiments mentioned in [15] have shown that the current density in pulsed discharges is in the order of $\sim 10\ A\ cm^{-2}$, whereas AC DBDs show much smaller densities $\sim 10 - 100\ mA\ cm^{-2}$. Having such high current densities means that using DC pulsed power in the plasma electrodes can improve the energy deposition, electron density, and electron temperature. Moreover, since the pulse duration and repetition rate can be adjusted in ideal DC pulsed power supplies, nanosecond pulsed DC discharge presents a well-defined control over the discharge energy. For the final electrode system, this enables control over the temperature of the electrodes, as per requirement **MR.6**, and the reactive species concentration or generation rate (**MR.3**).

In a study conducted by J.M. Williamson et al. [16], the differences between DC pulsed and AC discharge were experimentally examined. Here it was observed that the average deposited power of short pulse plasma was about 2.5 times greater than for AC excited plasma for similar repetition rates and applied external voltages, as can be seen in Figure 3.3. R. Brandenburg [9] explains the increase in deposited power as follows. Due to the much higher voltage steepness in a pulse, the Townsend discharge phase of a plasma formation is limited by the pulse rise time. That is, less charges can accumulate before breakdown. The Townsend mechanism is therefore shorter. However, the discharge voltage is increased, which leads to a larger amount of deposited energy and more charge transferred. Thus, the total charge carrier generation is enhanced during the first stages of a breakdown. As discussed in Section 3.2, the reduced electric field (E/N) value determines whether a discharge will occur. Since more energy is deposited, this value will increase for the same input of power. Furthermore, pulsed DC DBD will have lower gas heating and higher ozone (O_3) production because higher E/N. The increase in ozone is due to the fact that the ozone generation decreases with temperature, whilst ozone destruction increases with temperature [16]. For AC excited DBD, the gas temperature rises faster and the deposited energy is lower. These effects combined attribute to the advantage pulsed DC dielectric barrier discharge has over AC excited DBD in terms of ozone production (see Figure 3.4), which is the primary ROS used for disinfection.

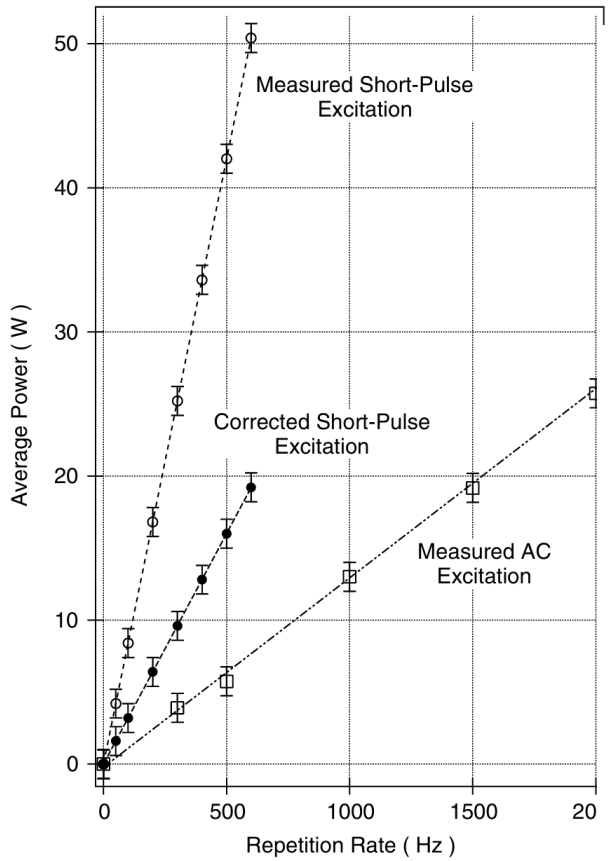

Figure 3.3: Average deposited power for AC and short-pulse DC excited discharges as a function of repetition rate, adopted from [16]

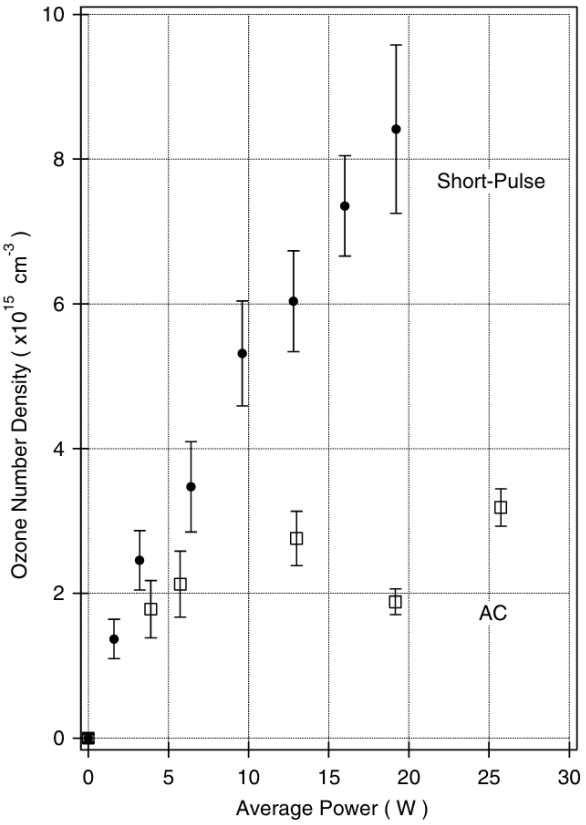

Figure 3.4: Ozone density as a function of deposited power, adopted from [16]

3.3. Reactive Species Generation for Disinfection

3.3.1. Reactive Species

In order to create reactive species, multiple plasma parameters can be considered: applied voltage, gas type, treatment time, relative humidity, and plasma exposure direction (indirect or direct). S. Patil et al. [19] summarised a lot of studies which experimented with the efficacy of reactive species. As was mentioned earlier in Section 1.2, plasma creates multiple ROS, RNS, and UV photons. These antimicrobial agents enable attacking multiple cellular targets, making non-thermal plasma highly effective for inactivation. For DBD plasma, it was found that in dry air ozone (O_3) was the main contributor to the sterilisation besides of UV. On the other hand, in moisturised air, OH radicals were the most effective. Another study mentioned in the chapter of [19] claimed that NO, NO_x and H_2O_2 were also effective for bacterial inactivation besides the radicals and ozone. That is because these reactive species impact the outermost membranes and cell walls of the treated microorganisms.

Thus, focusing on ozone production with plasma creation and thereby the design of the electrodes is of great interest to obtain the best microbial inactivation. Furthermore, humid air could be interesting for more effectiveness, although it could also cause electrode degradation over time when the relative humidity is too high [20]. Lastly, it contributes to the requirement to obtain a great disinfection effect in a short period of time with the final product in the fluidized bed, as per requirement **MR.11**.

3.3.2. Effect on Seeds

As was anticipated in Section 1.2, nonthermal plasma can have great effects on the decontamination of seeds. However, other studies have shown that the sterilisation effects are dependent on the gas used, exposure duration and the type of contaminated seeds. More specifically, the shape and surface

of the seed type play a major role in the disinfection effect of cold plasma [21]. On the other hand, the type of bacterial or fungi microorganism that is on the seeds require different types of treatment to obtain optimal effect. The main problem in seed disinfection is killing the strongest seedborne microorganisms. Usually these bacteria and fungi have thicker cell walls. From the review study conducted by J. Mravlje [22], it could be seen that the most resistive species that were tested by different research groups required overall the longest treatment time. In particular, one of the referenced studies experimented on the effect of cold plasma on one of the most resistive microorganism Alternaria, and showed that the infection degree decreased down to about 10% for a $300\,s$ treatment time [23]. In this work, a surface DBD was used with ambient air as discharge gas and maize seeds as contaminated objects. In other studies, the effect on different seedborne fungi was investigated and exhibited promising reduction results of fungi species [24] [25]. However, as mentioned in [22], the effectiveness on the type of seed (plant species), storage conditions, and also on environmental factors. Thus, for effective decontamination using cold plasma, specific treatment procedures for different seeds and different microorganism inactivation should be developed.

The plasma mechanism that causes the sterilisation effect results in non-linear survival curve shapes contrary to conventional sterilisation methods. This indicates that the cold plasma disinfection method is complex in terms of its influential factors. What is known is that direct exposure treatment leads to shorter sterilisation times and an indirect plasma exposure is safer, easier, and cheaper to operate [22]. Furthermore, there is a difference between low pressure gas plasma and atmospheric pressure plasma in terms of disinfection factors. Namely, for low pressure plasmas the UV radiation has a more significant effect than for atmospheric pressure plasmas. That is because the gas mixture for atmospheric pressure plasma does not generate UV photons of the correct wavelength for deep cell wall penetration of the microorganisms. Atmospheric pressure plasma relies mainly on the gas-phase molecule collisions for the reactive species generation where due to the higher pressure, a wider range of active species can be generated for microbial inactivation. Lastly, the chosen discharge gas is important for the disinfecting effect. Oxygen-containing plasma gas mixtures are preferred, as in previous research it was found that the created oxygen radicals had the most significant effect on survival rate reduction [22]. Even more so, the humid gas mixtures could have an even stronger disinfection effect, due to the formation of OH radicals. The combined effects of the cold atmospheric pressure air plasma radicals on seedborne pathogens can be described as follows. The OH damages the external structure of bacteria, the ozone (O_3) interferes with cellular respiration and the nitrogen atoms in air form NO and NO_x, which lead to the lethality of the microorganism in the plasma decontamination process [22]. Though the effectiveness of cold plasma on fungi has not been achieved on the same level as for bacteria, as these type of microorganisms typically have stronger cell walls [26]. To decontaminate seeds from invasive fungi, longer treatment times or stronger plasma formations are required to obtain a significant result [21].

For cold plasma, it has also been observed to have effects on the seed's germination. Though again, it is quite seed dependent whether or not the germination is enhanced or even decreased in some cases. Additionally, the germination enhancement has been observed by Y. Meng et al. [27] to be dependent on the type of gas used for plasma generation. From their experiment, it was observed that an air gas mixture had a positive effect on germination, just coming short on pure nitrogen N_2 and argon Ar gas. Moreover, the improved germination of seeds by cold plasma could be attributed to the increased water uptake due to the seed's surface oxidation [22]. However, care must be taken when aiming for decontamination of fungi on seeds, as the typically longer required treatment time could lead to adverse effects of seed germination.

Thus, as per requirement **MR.3.2**, the produced reactive species do not have directly negative effects, but rather their exposure time and intensity. In addition, since atmospheric pressure air is sufficient for both sterilisation and germination enhancement, requirement **MR.5** can be satisfied, together with the treatment effectiveness requirement **MR.11**.

4

Design Principles of DBD Electrodes

The main objective of the DBD electrodes is to optimise the plasma generation within the given size and power requirements. In the design two main design choices are made namely the types of materials used and the shape. In the design of either choice, a couple of additional factors are also taken into account. For example, electrodes also need to be durable and scalable as per requirements **MR.4**, **MR.8** and **ToR.8** Additionally, easy manufacturing and scalability of the electrodes is preferred since laborious manufacturing would mean high production cost or long times to create the electrodes or to scale up (**ToR.7** and **ToR.8**). For the final user, it is also important that the design allows modular implementation in the fluidized bed (**MR.1**, **MR.10** and **ToR.3**) and is safe and clear to use by the operator (**MR.9** and **ToR.6**).

4.1. Material Selection

The DBD electrode consist of two electrodes and a dielectric barrier. The electrodes are two conductors, one with a high voltage applied and one grounded electrode. Both electrodes together allow for a charge separation over the air gap. Meanwhile, the dielectric barrier should prevent these charges from exchanging between the two plates, blocking any short circuits and gives a self-extinguishing behaviour to the plasma. This is important to ensure low temperatures and low current (low power).

In this research multiple types of dielectric materials have been examined. However, the main types examined are PET and epoxy resin. Because of their high resilience to reactive species and accessibility. Epoxy can be easily poured into any shape and requires a voltage over $200\,kV/mm$ (DC) and about $100\,kV/mm$ ($3-5\,kHz$, AC) for breakdown. This is well above the supply voltage [28], [29]. PET has a lower breakdown voltage compared to that of epoxy and has a minimum DC breakdown at $68.8\,kV/mm$ and quickly dropped to $31.4\ kV/mm$ at $50\ Hz$ AC [30]. Different materials were examined in the paper by A. A. Garamoon et al. [31]. Some of the materials mentioned in that study are promising, such as the ceramic material Al_2O_3, but are more expensive, difficult acquire or to produce in the right shape.

As for the electrodes itself, the material should be able to carry the charges, for which conductors are used. The main parameters in choosing the conductors are the reactivity, workability, affordability and accessibility. In the choice of material for the electrodes workability and accessibility had a higher weight. Copper and aluminium are the main choices as the conductor material in this study. Copper was chosen because of its abundance in electrical components, making it easy to access and apply, which was later used in the shaping of the PCBs. Aluminium was chosen because of its ability to be able to laser cut it into preferred shapes, which is not possible for copper because of the high reflection of copper. Lastly, gold coated tungsten wires were chosen, as it is often applied in machines that make controlled electrical discharges [32].

4.2. Geometrical Considerations

The geometrical shape can change a lot about the performance of the electrodes. Since the plasma will be formed at the places where the electric field lines through air are strong enough to cause breakdown

of the air.
In this research, several types of DBD electrodes were examined. Wire electrodes, multi-hollow surface electrodes and Copper plates. The wire configurations will create a volume DBD discharge consisting of two set-ups; a wire-to-wire configuration and a wire-to-sheet configuration.

4.2.1. Wire Electrodes

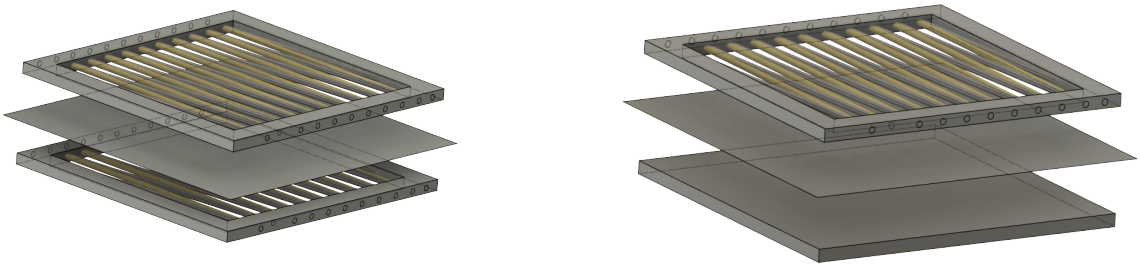

(a) Wire to Wire Electrode **(b)** Wire to Sheet Electrode

Figure 4.1: Wire-Electrodes

In the wire to wire configuration in Figure 4.1a, two frames are wrapped with a conducting wire and then placed in an on top of each other with a dielectric in between. One wireframe is the positive electrode and the other frame is the negative electrode of the DBD. In this research, the wire consists of a gold-coated tungsten (AuW) wire ($\sim 0.3\,mm$) and a PET dielectric sheet ($\sim 0.1\,mm$). The wire-to-sheet solution consists of just one wrapped frame placed on top of an aluminium sheet with a PET dielectric again in between. On the electrode frames, the spacing between the wires can be adjusted to have wider gaps or to have asymmetric wire placement between the top and bottom electrode. Lastly, the dielectric layer can be reconfigured with multiple layers of the same dielectric.

The advantage of the wire-to-wire electrode design with respect to the requirements is that dirt and dust will not accumulate (**ToR.5**) and that the open design will allow air to flow through the wires (**ToR.1**). However, it will be harder to have many plasma regions (**ToR.2**) and it is questionable whether the wires are durable enough to withstand impact (**ToR.4**). Indeed, the wire-to-sheet electrodes miss the advantages of no dirt accumulation and improved airflow, but they will be easier to configure and have better plasma generation because of the large ground electrode compared to the wire-to-wire.

4.2.2. Multi-hollow Electrode

The next considered design is the multi-hollow DBD (MHDBD) electrode. This is still a novel technique of creating cold plasma DBD. The principle of this configuration is to create plasma inside the holes of a plate. Here, the positive and negative electrodes are embedded in a dielectric, also in the inner walls of the holes, as can be seen in Figure 4.2b. Several studies have been conducted experimenting with the plasma formation for different voltages, frequencies and airflow rates through holes [33], [34], [35] and [36]. The interest in the MHDBD electrode configuration comes from the fact that it could be used as an air diffuser for the fluidized bed. In this way, the electrode could serve two required functions in one. Looking at requirement **ToR.1**, the MHDBD has no interference with the seed fluidization. When the final design has embedded electrodes, as is suggested by the previous mentioned authors, the design should be able to withstand seed impacts (**ToR.4**). Furthermore, it eliminates the need for separate electrodes inside the reactor chamber where the seeds will be fluidized and no debris will build up (**ToR.5**). The MHDBD diffuser would then be placed at the bottom of the chamber. The air flowing through the diffuser will become ionised due to the plasma formation in the holes and carry the reactive species to the seeds inside the reactor. Furthermore, additional characteristics of MHDBD are that the plasma electrodes are more cooled with higher flow rates [34], [33], [35]. However, Cimerman et al.

[35] also mentions that the emission intensity is slightly reduced for larger flow rates compared to still air at the same input power. In Figure 4.3, the experimental design for a MHDBD is shown. To analyse the effect of different hole diameters, various sizes were created in the design.

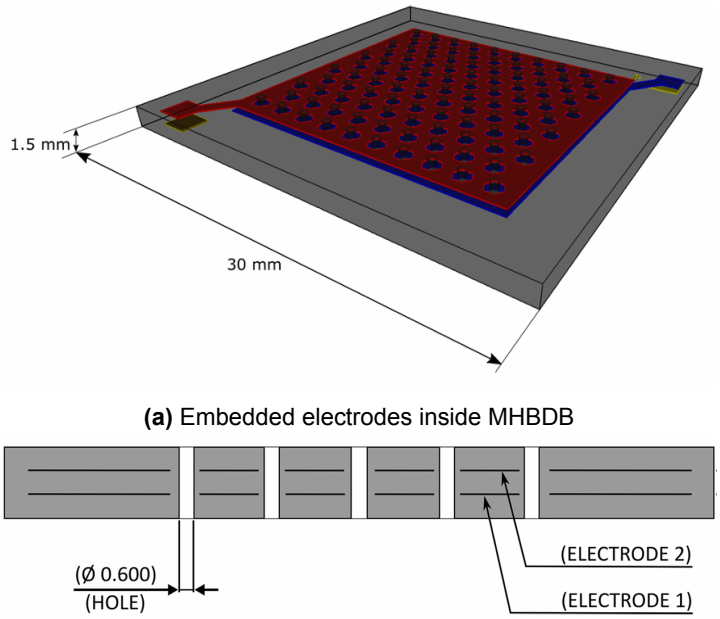

(a) Embedded electrodes inside MHBDB

(b) MHDBD side view

Figure 4.2: Visualisation of final MHDBD design, both adopted from [33]

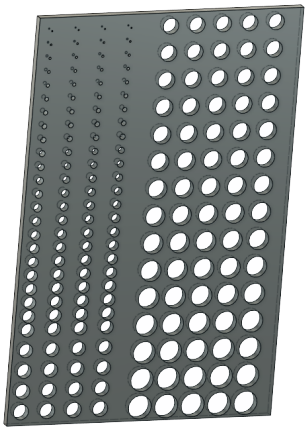

Figure 4.3: Multi-Hollow sheet Electrode

4.2.3. Copper Fractal Electrodes

Finally, copper fractal plate configurations were investigated. The used copper plates consist of either a single-sided or double-sided cladded copper layer with an epoxy layer in between [37]. The epoxy in the copper plates allow for a very strong dielectric barrier and the thin copper layer can modified through various manufacturing techniques (see next Section 4.3) to create the desired electrode pattern. The DBD configuration principles that are analysed in this section are the surface DBD (SDBD) and the coplanar DBD, which were described in Section 1.2.

Since most of the plasma forms around the edges of the conductor it is preferred to reach the longest line on a surface [38]. More specifically, in order to obtain the most plasma per area a space-filling fractal is proposed, which is desired as per requirement **ToR.2**. The property of these type of fractals is the large traversed path length to surface ratio. Furthermore, the exact definition of a space-filling curve is can be described as follows. One starts with a generator function, indicating the order of traversal in the initial domain, usually a unit square. Next, produce a new iterations by successfully subdividing the domain similarly as the generator function started the curve. However, every new subdivided domain should be connected in a way such that it is a rotated or reflected version of the generator function. By doing so, the neighbourhood and inclusion properties of such a curve are satisfied. Performing this procedure recursively, it has been proven that the fractal will completely fill the given domain and result in a self-filling curve [39]. In this report, the focus was set on the Hilbert and Peano fractals, which are shown in Figure 4.4. To create a SDBD out of the fractal, the fractal curve can be electrified conductor and the remainder of the surface the dielectric. The inverse is also possible, with the curve becoming dielectric and the remaining surface a conductor. The advantage of such curves is that the electric fields always point orthogonally outward from the electrode curve, creating strong fields at the sharp corners [40]. This localised enhanced electric field could lead to faster plasma generation in these locations. Regarding the latter statement, the Hilbert curve will be the preferred choice, as it contains more corners than the Peano fractal in the same area.

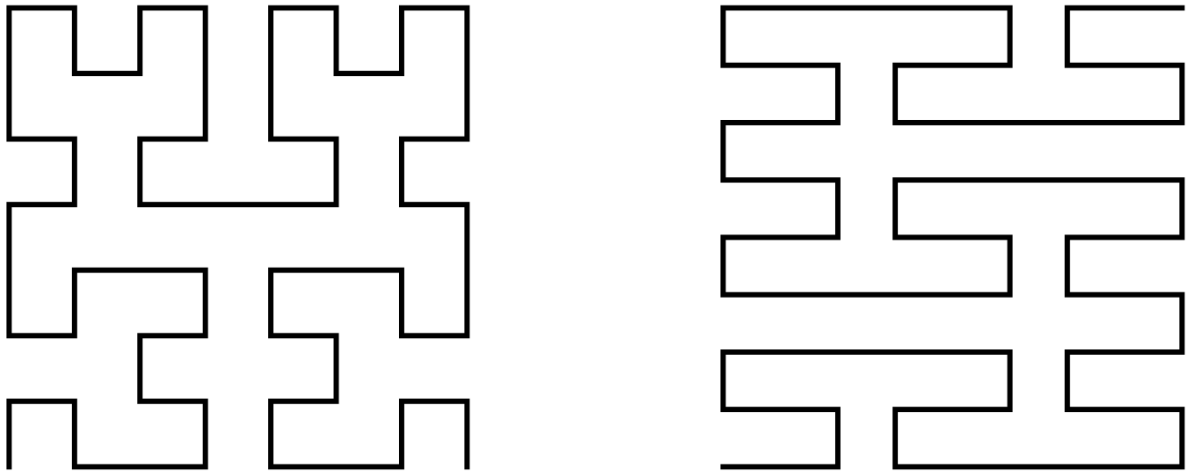

(a) Hilbert fractal third order **(b)** Peano fractal second order

Figure 4.4: Hilbert and Peano space-filling curves

Essentially, the higher the order of the fractal, the more dense the area will be filled with curved electrode paths. Obtaining a higher-order plasma fractal electrode could therefore be desirable to generate the most plasma per area, as has been set as a requirement **ToR.2**. Furthermore, the electrode could be made using a single-sided fractal and a full-sized ground conductor at the backside of the dielectric, or a double-sided fractal using the two-sided copper-cladded plate. Ideally, a plasma discharge will occur through the air gap on the positive side and on the grounded back side. Optimisation of the front and backside electrodes will be investigated in Section 5.2 by investigating the best placement to obtain the strongest electric fields. Figure 4.5 gives an illustration of where the plasma will be formed for the single-sided and double-sided fractal respectively. Note that in Figure 4.5b, the bottom electrode can optionally be embedded in the dielectric or exposed at the bottom to air. As for drawbacks of this design, the electrodes do not allow for air to flow (**ToR.1**) and could possibly have dirt and debris build up over time (**ToR.5**), depending on the implementation in the fluidized bed.

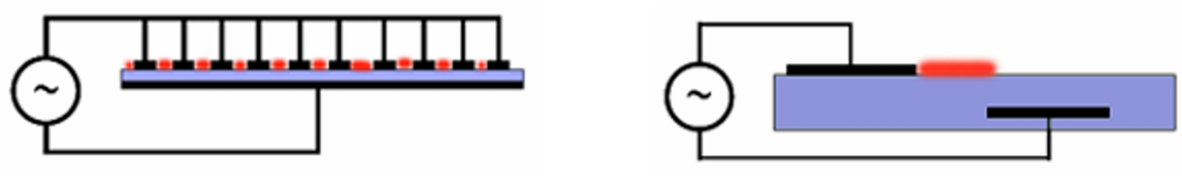

(a) Single-sided SDBD fractal

(b) Double-sided SDBD fractal

Figure 4.5: Side-view showing the plasma formation of both configurations, adopted from [41]

Coplanar electrodes are a distinct type of DBD in the sense that their positive and negative or grounded electrode are on the same horizontal line (see Figure 4.6b). Furthermore, both conductive terminals will have to be embedded in a dielectric material to prevent direct discharge in air between them. This type of electrode can be realised again using a Hilbert space-filling curve, as can be seen in the top-view representation in Figure 4.6a. With this design, it can be ensured that the electrode is well isolated from the surrounding air. This means that debris build up will be minimal (**ToR.5** whilst using a space-filling curve (**ToR.2**).

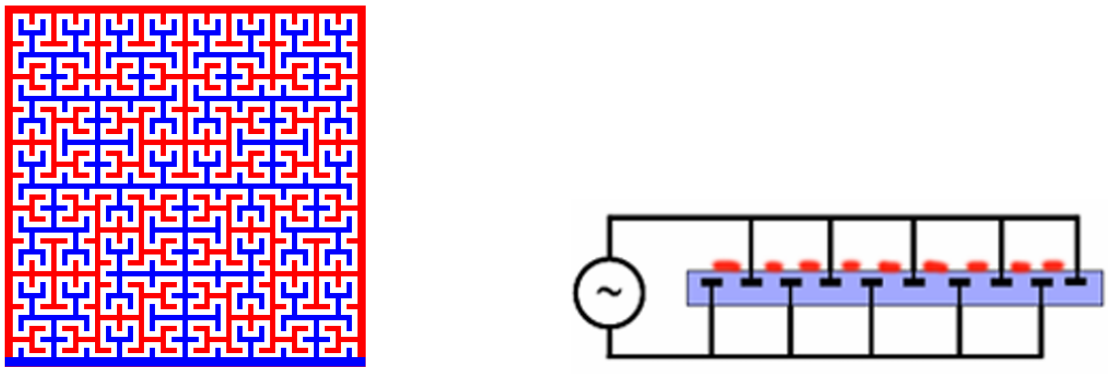

(a) Coplanar 5th order Hilbert, white is dielectric, red is positive and blue is negative polarity

(b) Side-view showing plasma formation for coplanar configuration, adopted from [41]

Figure 4.6: Coplanar electrode

4.2.4. Capacitance

Since the electrodes consist of two conductors with an insulation between them, it acts as a capacitor. The formula for a capacitor is:

$$C = \epsilon_0 \cdot \epsilon_r \cdot \frac{A}{d} \, [F] \tag{4.1}$$

With C the capacitance of the electrodes in Farad, ϵ the permittivity of the dielectric, A the effective surface and d the distance between the plates. when calculating for the capacitance of copper-epoxy fractal electrode, which covers half the area, the resulting capacitance for a $10 \times 10 \; cm$ plate with an epoxy resin having a relative permittivity of 3.6 [42] and $1.6 \; mm$ thick is around $100 \; pF$. Note that the area of the original plate is halved and that the measured capacitance might differ due to fringing effects caused by the cut out grooves of the SDBD fractal electrodes. Additionally, the capacitance can be used to determine the degradation of the electrodes itself. This is because micro discharges might damage the dielectric barrier, which is responsible for preventing short circuits, thereby lowering the internal resistance and thus the the capacitance.

4.3. Electrode Fabrication and Electrical Safety

After the materials and configurations are chosen, the manufacturing method should be considered. Applicable methods for creating the plasma electrodes include additive manufacturing (AM) techniques, laser cutting or CNC engraving.

To begin with the wire-electrodes, their frames could be fabricated using a laser cutting machine to produce the right size of frames and mounting points for the wires. The frame could be any non-conducting material like acrylic polymer (PMMA) and cut using a laser cutter. The wires are then wrapped around the frame and securely mounted. Only the dielectric material would have to be applied between the ground and live wires of this electrode setup. More specifically the grounding sheet of the wire-to-wire electrode could be made from aluminium tape directly applied to the backside of the dielectric material.

Secondly, the hollow-sheet electrode experimental design could be produced via laser cutting aluminium. Using laser cutting, fine precision of the different holes can be achieved. To secure the stacked positioning of the grounded and live electrode, a frame with mounding screws could be 3D-printed using thermally resistive and non-conducting material. In between the two aluminium plates, a dielectric of a certain thickness can be placed.

Next, the fractal design could be implemented using multiple additive manufacturing and engraving methods. Since the fractal electrodes require more precision in manufacturing, one could think of accurate manufacturing techniques like inkjet printing with conductive ink on a dielectric. Such a method has been attempted by J. Kim et al. [43] to create flexible dielectric barrier discharge (FXDBD). Here, a PET substrate was used to print on with commercial silver nanoparticle ink by using a normal office printer. This could be a great solution regarding workability, affordability and accessibility. However, the issue with printing the electrodes is that the applied conductive layer on the dielectric suffers significantly to degradation due to the plasma particles. To overcome this issue, multiple conductive ink layers could be printed or a protective layer could be added over the entire surface. J. Kim et al. [43] covered their electrodes with a transparent silicon layer and noted that this improved the lifetime significantly. Though, from the conducted experiment in this report, it was found that the lifetime of the FXDBD was just over two hours of continuous use. Overall, the conductive inkjet printing method is promising from the manufacturing point of view, but it is questionable whether the produced electrodes will have a long enough lifespan for multiple uses.

Besides from inkjet printing, the additive manufacturing process of powder bed fusion could be applicable to create the metal lining for the electrode fractals. In a personal conversation with Dr. ir. M.J.M. Hermans from the TU Delft faculty Mechanical Engineering this method was discussed. According to Hermans, a metal powder can be applied to a surface using powder bed fusion where layer by layer the powder can be applied with a adhesive material in between. However, in the final sintering process of this method, the created object suffers from a shrinkage of $10 - 20\%$ of the initial volume. Additionally, the sintering process uses high temperatures to about $800°C$, which the substrate dielectric layer must also withstand.

As for the last fabrication method, CNC engraving on a PCB copper cladded prototyping board with an epoxy dielectric layer [37] was investigated. These prototyping boards are readily available at hardware or electronic stores and have a good dielectric material and conductive layer all in one affordable package. Additionally, the great accessibility to a CNC machine during this project made fast and affordable prototyping possible. The fractals could be milled out using different drill-heads and with sufficient precision. However, the downside of drilling is that the cut out corners become less sharp than with laser engraving.

Finally, when implementing the electrodes into the fluidized bed, it must be taken care of that the positive voltage and grounded or negative voltage connections are spaced at maximum distance as possible from each other. This is because otherwise a discharge arc could occur directly between the connection cables or over the outer edge of the electrode. Grounding the electrode after a disinfection procedure is also of great importance to ensure any static charges trapped in the dielectric layer are removed. The connections for this can be made using conventional crocodile or banana plugs. This is demanded by requirements **MR.9** and **MR.10**. Additionally, in order to avoid spark formation via the outer edges of the electrode, the borders should be of a great enough distance such that the shortest path length for plasma is always through the dielectric, as is part of requirement **MR.4**. The electrode size is constrained by the requirements **MR.1** and partially by **ToR.1** and thus the outer edges should always be a dielectric and included in the sizing of the final design.

5

Measurement Techniques and Modelling

In order to determine whether the designs will work it is important to make a testing and modelling setup. The models can be made are made in the COMSOL AC/DC module [44], in order to simulate and plot the electrical field lines for different electrode size parameters. The measurements are done in the High Voltage lab of the TU Delft to guarantee safety.

5.1. Test set-up

The test setup consists of the electrodes, a high voltage (HV) source and a reference capacitor. In this test, a $50\ Hz$ variable AC HV source was used with a maximum output voltage of about $20\ kV$. The rest of circuit was connected as per the schematic in Figure 5.1. With two HV probes placed over the circuit, one at the output of the transformer (HV-source) and one over a reference capacitor. In the measuring set-up a reference capacitor of $100\ nF$ was used. This value could arbitrarily chosen. However, it has to be much larger than the electrode capacitance in order to have few interference from the capacitor itself. Since with two capacitors in series and one being much larger then the other the equivalent capacitance almost equals that of the lower one.

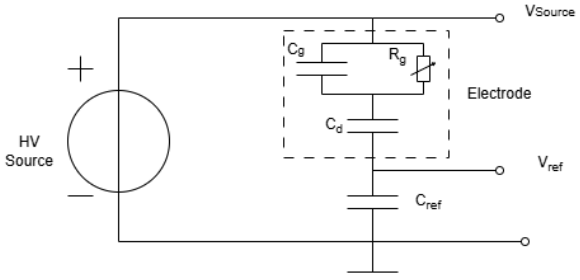

Figure 5.1: Schematic Test Set-up

In order to determine the charge, the voltage over the reference capacitor is measured. The charge in a series connection must be the same. This is due to charge neutrality in a closed system where charges on the positive plate are equal in magnitude to the accumulated charges on the negative plate on the same capacitor. For multiple capacitors in series, the total charge remains the same, but the equivalent capacitance is lowered in the closed circuit [45]. Therefore, the charge on the electrode can be determined from the charge of the reference capacitor using Equation 5.1. With the known capacitance of the reference capacitor and measured voltage over the capacitor the charge in the system is determined.

$$Q = C \cdot V \tag{5.1}$$

In Figure 5.1 is the electrode drawn as its equivalent circuit. With C_d being the capacitance between the dielectric surface and the encapsulated electrode, while C_g and R_g are the capacitance and

resistance between the exposed electrode and the dielectric surface, respectively. When a low voltage is applied, R_g is very large, leading to an approximated series connection between just C_g and C_d. However when plasma is generated, R_g drops and becomes dominant over C_g leading to a connection between just C_d and R_g [46]. Since R_g becomes dominant, the capacitor C_d becomes more active and dominant allowing for more current to flow through the circuit, thereby allowing for more voltage over C_{ref}.

By measuring both the reference voltage and source voltage, a time shift can be observed. By plotting both lines against each other the time component disappears and the delay between both signals returns as a shift in return, evidently separating both lines. Since R_g is inversely related to the plasma generation, meaning more plasma leads to a smaller value for R_g, is directly related to the phase shift. Since an ideal capacitor has an impedance of $\frac{1}{j\omega C}$, which corresponds to a phase shift of $-90°$. The figure will be maximally open, being either a circle or a square, depending on the size of the capacitor. However, when a real component is added (a resistor) this phase shift becomes less negative than $-90°$ (so $[-90, 0]$) leaving a smaller hole.

Since this shift is coming from the resistance of the plasma, this dissipates energy, which corresponds to the surface of the Lissajous figure [46]. Therefore, by integrating the Lissajous figure the surface area corresponds to the energy E put into the plasma per cycle. In order to find the power per cycle, the energy has to be multiplied by the frequency f of the high voltage source. For testing, the source will be put at maximum voltage before either breakdown of the electrode happens due to a high voltage or frequency. The formula that describes the energy per input pulse of the power supply is the following from H. Jiang et al. [46]:

$$E = \int Q \cdot dV = A_{Lissajous} \tag{5.2}$$

Based on this equation from the research paper, the power can be found as:

$$P = Ecycle \cdot f = A_{Lissajous} \cdot f \tag{5.3}$$

The analysis of the electrode data was done using Python. The integration procedure was carried out by splitting the Lissajous figure into different sections and applying the composite trapezoidal rule for each section, which is a numerical integration technique [47]. The figure itself was split into four sections as can be seen in Figure 5.2. With first being split up into two sections, the data points corresponding to $y > 0$ and $y < 0$. Then the end points of the Lissajous figure are determined to again split both lines into two sections again, resulting in four sections. Then for the values for $y > 0$ the upper curve (the orange line) is integrated with respect to zero to which the integrated to zero lower curve line (green) is subtracted from. For the values lower than zero this is flipped, so the purple integration is subtracted from the red curve. The reason why the integration could not be done in one run is because the upper and lower data points do not perfectly match in their x position and thus interpolation and integration in sections was required to obtain the area of the Lissajous figure.

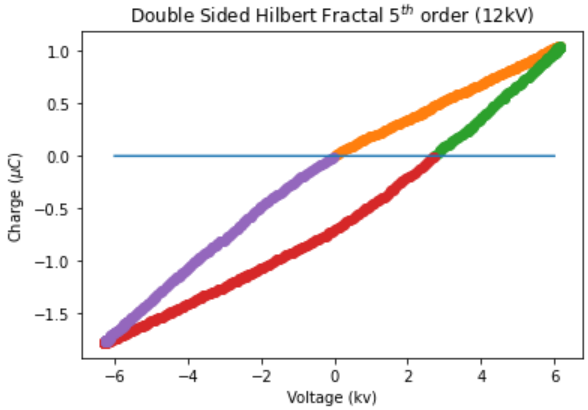

Figure 5.2: Illustration of integration

Finally, also visual images were made. To get visible pictures of plasma at low frequency, the images were taken in a box to reduce ambient light for the photo. A camera could then be placed trough an opening of the box to make long exposure pictures. In the this setup, the camera used is the main camera from an Iphone 13, where pictures were taken with a remote button to ensure safety during testing. In the end, the temperature was monitored using a the Voltcraft ir-270L laser-based temperature sensor.

5.2. Fractal Simulation in COMSOL

To obtain the optimal parameters for maximum electric field in the double-sided fractal electrode design, the placement of the copper conductors on the epoxy dielectric had to be simulated. The setup in COMSOL was made by placing copper segments with a minimum width of $0.5\ mm$ on the top and bottom side of the dielectric interchangeably. Next, the dielectric width was selected multiple orders larger than the electrode array width, such that simulated fringing effects via the edges through air would become negligible. The conductor, dielectric and surrounding segments were then specified with their respective material parameters from the COMSOL library. Furthermore, the electrical parameters were set such that the top copper segments were electrified with a voltage of $8000\ V$ and the bottom segments were set as ground. The choice for a specified voltage is not required for the simulation, as the optimisation is not aimed to achieve a certain electric field but only the copper width and spacing parameters. Though, since this value was the largest recorded value for breakdown in air, as was discussed in Section 3.1.1, this value was chosen as the electrode distance will be simulated in the sub-millimetre range. Next, the COMSOL study was configured with a parameter sweep. The iterated parameters in the simulation are the electrode width w_{elec}, horizontal spacing between top and bottom electrode d_{space} and the dielectric height d_{height}. In order to perform a selective study in COMSOL, a probe point had to be placed. The probe point was set at a close distance from the middle positive conductor, as can be seen in Figure 5.4. In the COMSOL study, it was then selected to measure the electric field at the probe point, after which the simulation could be performed. The simulation in COMSOL relies on a generated meshing grid (see Figure 5.5), in which finite element method solutions can be produced. When placing the probe point, a point was selected such that it does not coincides with many different grid planes, which would lead to unsolvable simulations.

The iterated values in the simulation were the electrode width, which was simulated from $0.5\ mm$ width to $2.0\ mm$ with increments of $0.1\ mm$. Simultaneously, the horizontal spacing between positive and ground conductor was swept from $0.0\ mm$ to $0.2\ mm$ with the same incremental step. The height was not iterated in this simulation, since it is expected that the main plasma formation will originate in the horizontal direction, as the electric field will be the strongest in that direction due to the asymmetric placement of the ground conductor. The result of the parameter sweep in COMSOL showed that the strongest electric field at the probe point was obtained for the widest electrode width and smallest spacing in between, as can be seen in Figure 5.6. Moreover, the electric field strength is the strongest at the corner edges of the electrodes and in the middle between two positive top electrodes the weakest. Though, in this middle point, the magnitude of the electric field is still around $5\ kV/mm$, as can be seen from Figure 5.4. Thus, it can be inferred from the simulation that the optimal double-sided electrode design must have the widest possible conductor widths per given area on both sides of the dielectric. Implementing this should guarantee that the maximum electric field will be formed on the given area according to the applied voltage. In the event that the electric field is too strong and shows filamentary discharges, the voltage can be reduced using the power supply to obtain microdischarges again.

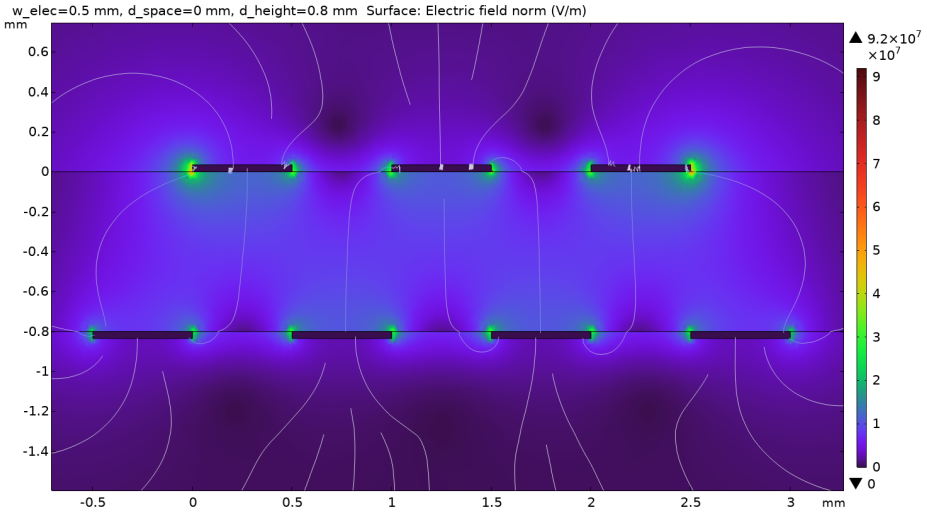

Figure 5.3: Electric field plot for optimised electrode parameters for a onset voltage of $8\ kV$, obtained by parameter sweep

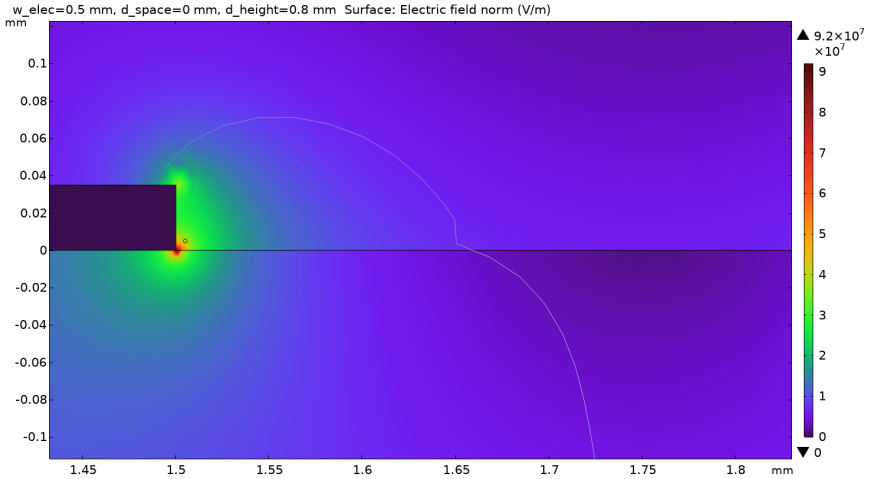

Figure 5.4: Electric field plot zoomed in on optimisation probe point close to one conductor

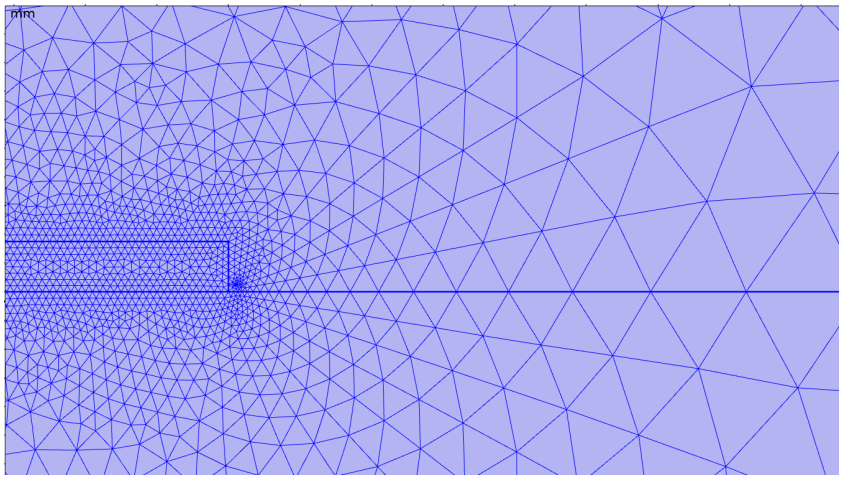

Figure 5.5: Meshing grid at probe point for simulation

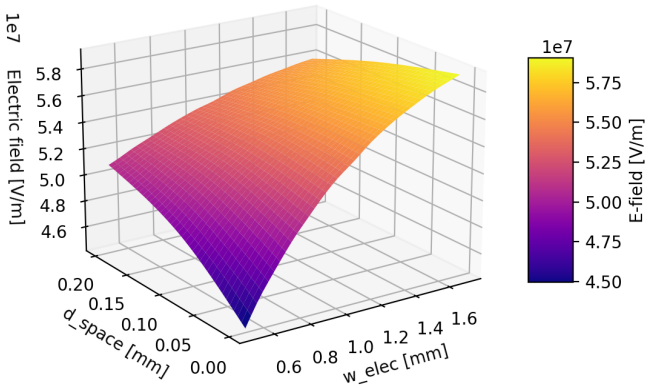

Figure 5.6: Simulated electrode parameters versus electric field intensity

6

Electrode Implementation and Testing Results

After various of tests were executed with the most important being the Lissajous figures obtained from the oscilloscope. The results from the oscilloscope are rather noisy as an example can be seen in Figure 6.1. In order to gain better quality figures a set of filters was applied to the signal. Since the amount of usefully data is in the lower frequency range of the signal (for surface electrodes $50\ Hz$) a set of low-pass filters was applied. With first a smoothing function which filters out extreme values, due to noise or errors from the oscilloscope. The function way this filter works is by taking the difference at two points and filtering out values with an extreme difference. Then it replaces it by averaging with the next value, smoothing the function and lowering the extremes. This filter is applied for 6 times following with an averaging of 500 samples. The reason for using two filters is to remove high peaks, and since this filter doesn't shorten the data array, this filter can be applied without losing data points, unlike the averaging filter.

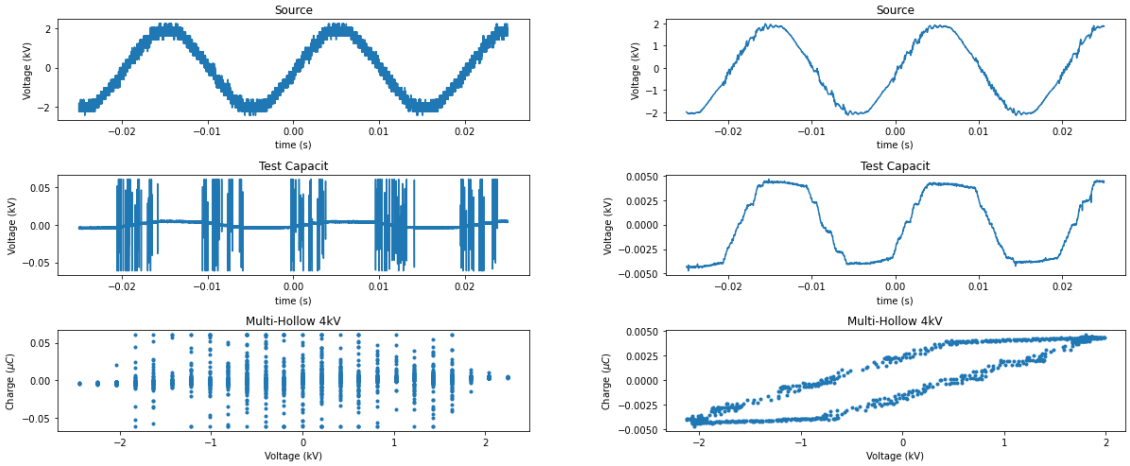

(a) Multi-Hollow unfiltered

(b) Multi-Hollow (filtered)

Figure 6.1: Filtered vs Unfiltered (Multi-Hollow)

Next in Figure 6.3 and Table 6.1 are the filtered python results from the measuring set-up. Note that not all types of electrodes are represented in the Lissajous figure. This is because some electrode failed, like the co-planar electrode or because they had horrible visual performance, like the Peano electrodes (Figure A.17). From the Lissajous Figure (6.3), it can be seen that the copperplate electrodes are in comparison way more stable then the build electrodes. The data points are more smoothly and closer spaced. It is also note worthy to add that some of the figures have a rather large offset. This happened when the electrodes came close to breakdown.

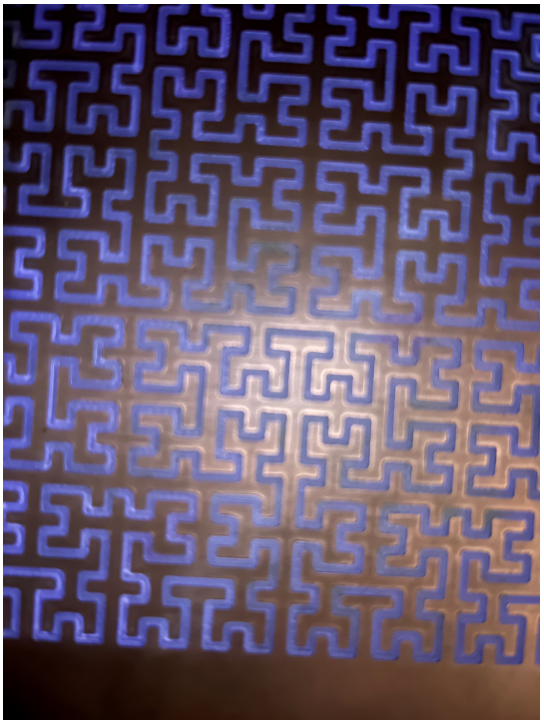

(a) Picture Hilbert 5^{th} order 1.6 mm

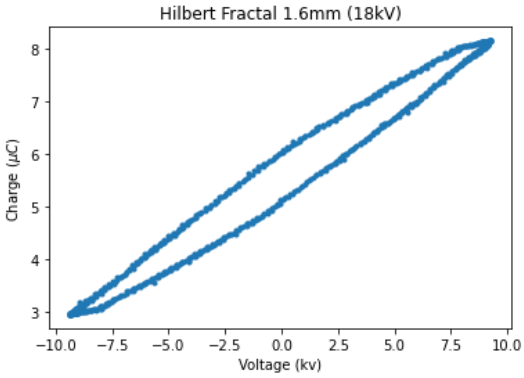

(b) Hilbert 5^{th} order 1.6 mm

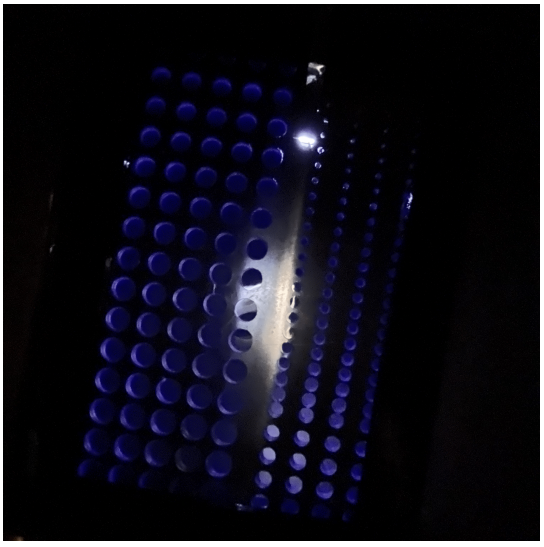

(c) Picture Multi-Hollow

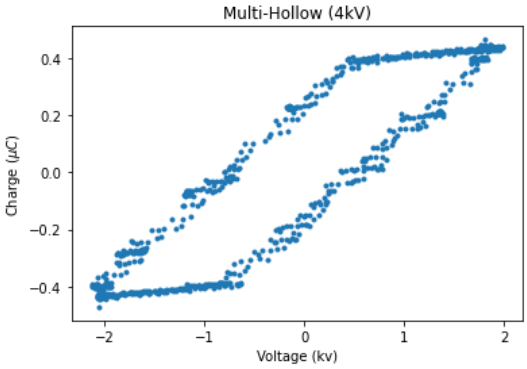

(d) Multi-Hollow (4kV)

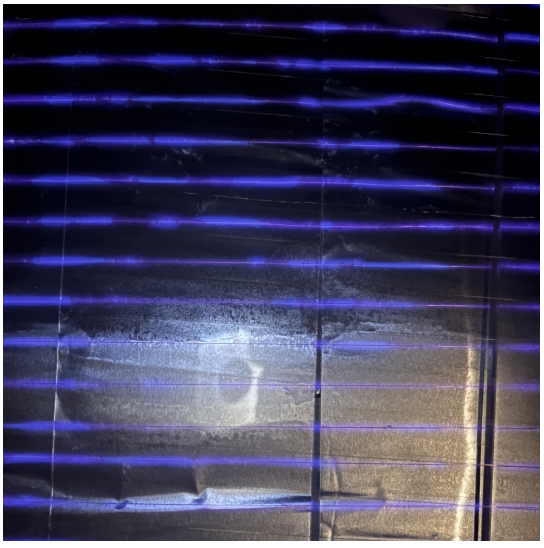

(e) Picture Wire to Sheet

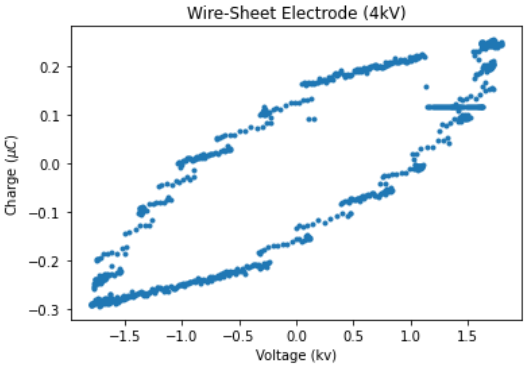

(f) Wire to Sheet Electrode

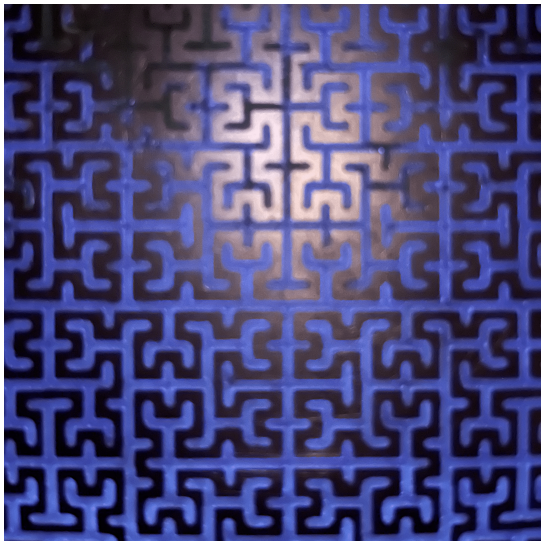

(a) Picture Double Sided Fractal (back side)

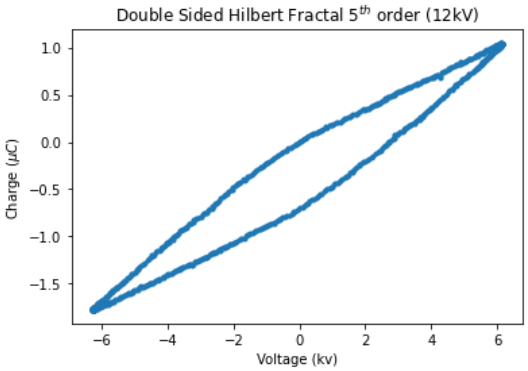

(b) Double-sided 5th order Hilbert

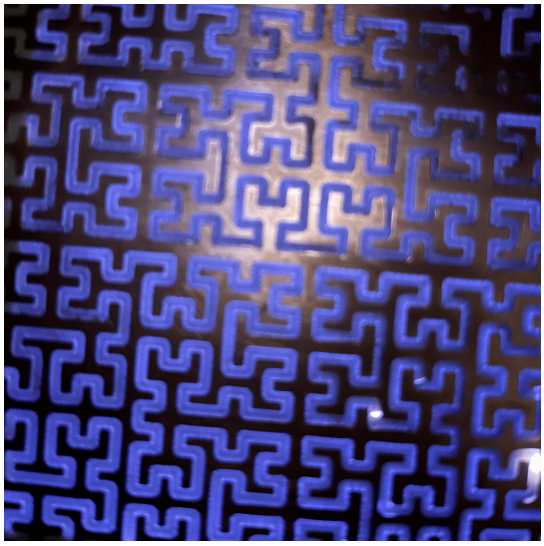

(c) Single-sided 5^{th} order Hilbert 0.8 mm

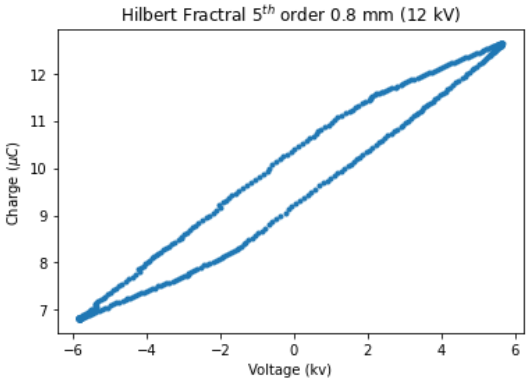

(d) Hilbert Fractal 0.8 mm 5^{th} order (12kV)

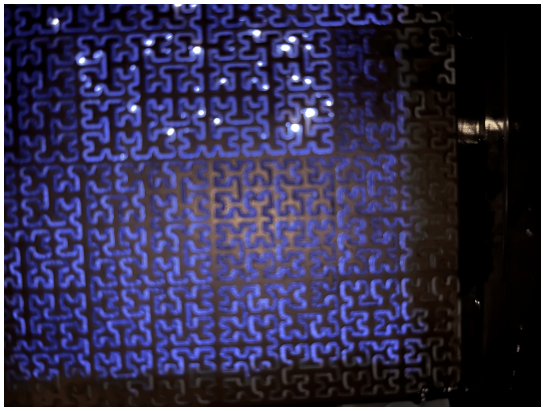

(e) Picture Single-sided 6^{th} order Hilbert

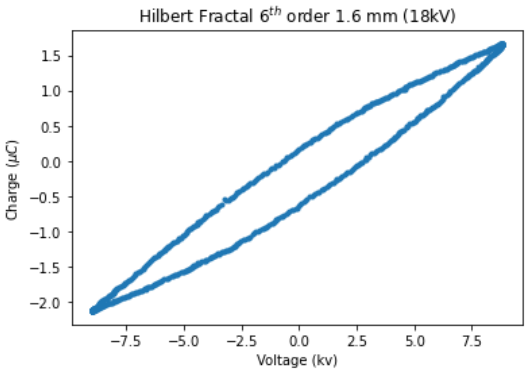

(f) Single-sided 6^{th} order Hilbert

Figure 6.3: Lissajous Figures & Plasma Pictures

In Table 6.1 the calculated results from the Python code can be observed that were calculated using Equation 5.3 that was adopted from [46]. Most electrodes were measured at approximately their maximum voltage before either breakdown or when the maximum voltage of the source was met. Important

observations that can be seen are that the higher the supply voltage the higher the plasma generation. However, there is a large variation in maximum voltage. This has to do with the geometrical design of the electrode or the thickness of the dielectric barrier. For example the pet-film based electrodes were limited at about $6\ kV$ and thereby had relatively small plasma generation, however still in trend with copperplate electrodes at the same voltage. However be aware that most of the copperplate electrodes had relatively high turn on voltage which can be seen in Table 6.2. However the copperplate electrodes were able withstand way higher voltages with no direct visible damages. Thereby allowing for higher plasma generation. With the main favourites being the Hilbert Fractal 5^{th} order single-sided $0.8\ mm$ dielectric barrier followed by the double-sided Hilbert fractal 5^{th} order and the single sided $1.6\ mm$ dielectric barrier 6^{th} order.

Electrode	Supply Voltage (kV)	Charge (μC)	Power (W)
Wire-Sheet	3.609	0.649	0.0351
Double Sided Hilbert fractal 5^{th} order 1.6 mm	12.461	2.833	0.2628
Hilbert Fractal 5^{th} order 0.8 mm	5.072	1.916	0.0599
Hilbert Fractal 6^{th} order 1.6 mm	9.915	1.749	0.089
Hilbert Fractal 6^{th} order 1.6 mm	17.877	3.816	0.4703
Multi-Hollow	4.118	0.935	0.0504
Hilbert Fractal 5^{th} order 0.8 mm	11.554	5.881	0.4533
Hilbert Fractal 5^{th} order 1.6 mm	18.693	5.210	0.5669
Hilbert fractal 5^{th} order 0.8 mm	4.727	1.766	0.03444

Table 6.1: Results Electrodes

In the table below the turn on voltage of various electrodes can be found. It is important to remark that determining the turn-on voltage is rather difficult because it is very difficult to determine when the first corona discharges happen. This might even happen at relatively low voltage, which is why the values in the table below are greatly approximated from when the Lissajous figures opened.

Electrode	Turn-On Voltage
Hilbert Fractal 5^{th} order 0.8 mm	$\sim 5kV$
Double Sided Hilbert fractal 5^{th} order 1.6 mm	$\sim 5kV$
Hilbert Fractal 6^{th} order 1.6 m	$\sim 3.4kV$
Multi-Hollow 1 PET Sheet	$\sim 3.5kV$
Multi-Hollow 2 PET Sheets	$\sim 4.5kV$

Table 6.2: Turn on voltages of various Electrodes

Finally, a quick temperature test on the electrode was done on both 50 Hz and once on $3\ kHz$. Under $50\ Hz$ no heating was observed. However on higher frequency this some heating was observed to be around $40 - 50°C$.

6.1. Additional Results on Germination Effect

After an additional performed test, two batches of seeds were send to the lab of the project proposer Bejo Zaden. One batch was treated using cold plasma generated by the electrodes for 15 minutes and one batch was untreated.

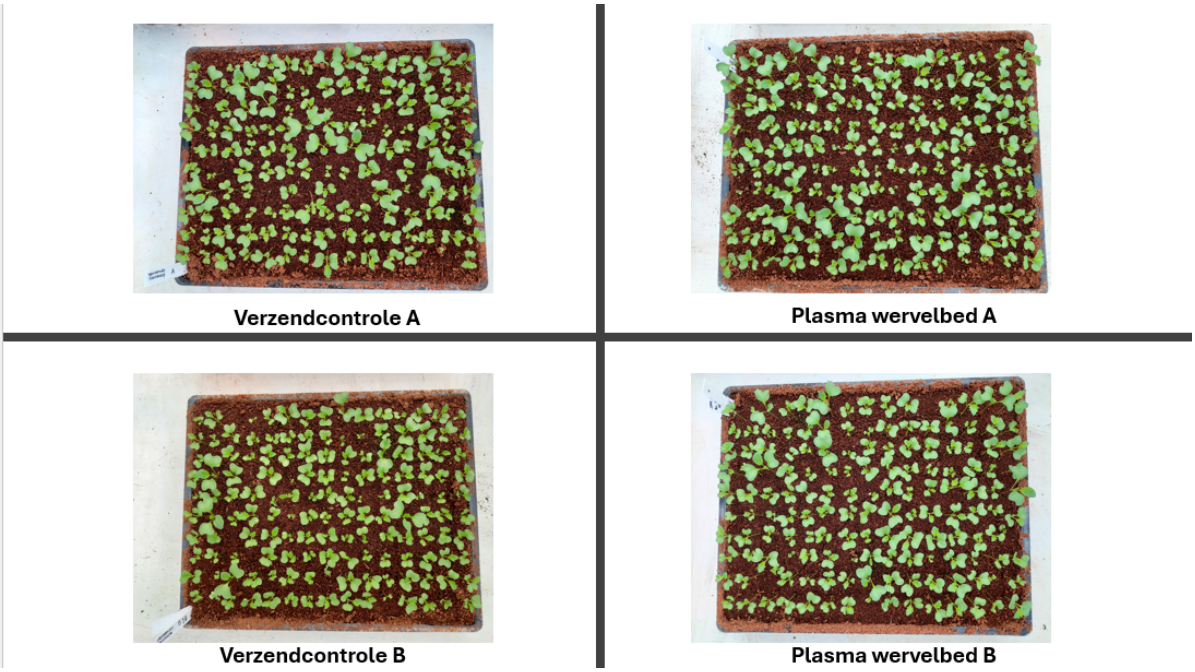

Figure 6.4: Germination results, left column is untreated, right column are the treated seeds

The test performed by Bejo Zaden showed that the germination of the treated seeds was 94% whilst the untreated seeds (the control group) was 91%. This can also be seen in Figure 6.4. The two groups of seeds consisted each of 150 seeds.

7

Discussion of the Results

From the tests, some important observations can be made. To start off, it is difficult to accurately measure plasma since many parameters play a role. For example, the effective area, temperature, humidity all have effect on the plasma formation. In this research the main two ways to measure plasma generation were done based on Lissajous figures and visual assessment using pictures taken on a shutter time of 30 seconds in a dark area.

From visual assessment, it was determined that the Hilbert fractal created better results than the Peano fractals (Figure A.17). This is most likely due to the fact that the Hilbert fractal has more edges, and thus creating stronger electric fields. Additionally, the double-sided Hilbert of $1.6\ mm$ and the single-sided $0.8\ mm$ showed strong plasma formation on the images. However, they had a lower breakdown compared to single sided $1.6\,mm$ electrodes, yet they still suffice the requirement to be able to operate on a maximum voltage of $10\,kV$. It was also observed that the $0.8\,mm$ had some strong points of discharge, creating plasma discharge visible even in daylight at $50\ Hz$. This is not ideal behaviour, and can be most likely be attributed to manufacturing issues, since milling on a $0.8\,mm$ thick barrier is more difficult than $1.6\ mm$, as it leaves less room for the drill to go into the board. However, this could be solved rather easy by having higher precision equipment. From visual observations could also be observed that all the electrodes were generating plasma at the entire surface of the electrode. Resulting into optimal use of the surface area for plasma generation.

As for the wire and MHDBD electrodes, they were made using tightening the wires by hand or securing the conducting plates with a handmade frame. Evidently, due to the manual work, those electrodes showed less optimal results. Both the wire electrodes as for the hollow surface electrode having dielectric breakdown around $7-8\,kV$. Which is below the required voltage. This could be resolved using a thicker dielectric barrier or a different stronger dielectric barrier. As of now, the PETG layer used in both electrodes showed a lot of degradation during testing (Figure A.6), which eventually would result into breakdown after a couple of uses, leading to high replacement rates of the electrodes.

Finally, the coplanar electrodes, these electrodes were made using a fractal design that was separated in a positive and negative voltage section. Both polarities were located on the same plane and coated with a dielectric barrier. These electrodes were created by milling the fractals onto a copper-cladded FR4 epoxy plate which was then coated again in a layer of epoxy resin creating the dielectric barrier. The final result resulted into having an epoxy layer of about $0.5\ mm$ thick. However the results were rather disappointing resulting into breakdown before visible plasma generation occurred.

From visual experiments, the best electrodes were the double-sided fractal, $0.8\,mm$ fractal and $1.6\,mm$ 5^{th} order Hilbert electrode. With the double-sided fractal generating the plasma on both sides of the electrode compared to that of the others. The $0.8\ mm$ created the strongest intensity plasma and the $1.6\ mm\ 5^{th}$ order Hilbert electrode the most diffuse plasma. This however was not entirely backed by the calculated data. Which indicated the $1.6mm\ 6^{th}$ order Hilbert electrode performed the best, then the $0.8\ mm\ 5^{th}$ order Hilbert electrode and then the $1.6\ mm\ 5^{th}$ order Hilbert electrode. Some similarities

are found, however, the main difference between the two methods is that no electrodes were equally sized in plasma area. This lead to to some electrodes having more area for plasma generation thus scoring better on the results of electrode, which should be taken into consideration when creating the electrode in order to satisfy all the trade-off requirements mentioned in Section 2.3. Therefore the final top three types of electrodes are: the double-sided Hilbert fractal, $0.8\ mm\ 5^{th}$ order Hilbert electrode and $1.6\ mm\ 6^{th}$ order Hilbert electrode. The most optimal electrode would probably a combination of these three, as they all have favourable properties. That is, according to the trade-off requirements, all electrodes show plasma generation below $10\ kV$, do not show sparks when manufactured carefully, and have the most plasma generation per area. Thus, the most optimal design would be a double-sided $0.8\ mm$ thick dielectric 6^{th} order Hilbert electrode.

8

Conclusions and Recommendations

In this study, a design procedure has been described for the construction of cold plasma DBD electrodes for seed disinfection, based on a series of mandatory and trade-off requirements. Plasma, being the fourth state of matter, is initialised by different breakdown mechanisms. Moreover, when a breakdown will occur could be discovered from the empirically defined Paschen curve and the ionisation by the Townsend breakdown process. Whereas Townsend breakdown produces diffuse plasma of low-current, DBD actually produces plasma streamers, which collapse after a short time due to a formation of an opposing electric field. This so-called self-extinguishing behaviour provided the motivation to use DBD electrodes to produce cold plasma. That is because the formed plasma gases have disinfecting properties on seedborne pathogens. Through literature, it was discovered that ozone (O_3) was the main reactive agent in atmospheric pressure air plasma that could sterilise microorganisms on seeds. Furthermore, it was found that the most power efficient ozone generation could be achieved by short-pulsed excited DC dielectric barrier discharges. The generated cold plasma did not only contain ozone, but also other reactive species such as OH, NO, NO_x radicals. Each produced chemical had their own effect in the disinfection process and for some seeds, the plasma exposure could lead to improved germination according to several studies.

After the theory was understood, several designs were proposed. First, the type of materials were considered for the electrodes. Next, geometrical considerations were made based on the requirements. From the geometrical considerations, five designs originated, some being slight alterations of each other. The wire electrode designs favoured airflow and less debris build up for in the fluidized bed, whereas the multi-hollow DBD electrode presumed to be a all in one solution, but was harder to produce and have a thick enough dielectric barrier. Lastly, the space-filling curve electrodes using the Hilbert and Peano fractals were considered. These electrodes had as design advantage that they had the larges discharge area and were easy to fabricate. The coplanar design alteration also had better insulation than the other electrode designs. However, the double-sided fractal seemed promising because plasma could be formed on both sides on the electrodes, which was beneficial for the implementation in the fluidized bed. Many manufacturing methods for the different designs were investigated, but overall the most accessible and readily used materials were chosen such as copper and aluminium for the conductor and PET and epoxy resin for the dielectric. Lastly, laser-cutters and CNC machines were used to create the electrodes or their frames.

For testing the electrode designs a test setup was made based on the commonly used Lissajous figure method. In the testing procedure, a reference capacitor was placed in series with the tested electrode. The voltage drop over the capacitor could then be measured and plotted together with the input voltage into a Lissajous figure. To make the model complete, the voltage drop over the reference capacitor had to be multiplied with the reference capacitance to obtain the charge. In this way, the area of the Lissajous figure functioned as a measure of power and could be used to determine the power of every electrode design. Though, alongside a physical testing setup, a COMSOL simulation was made to improve the double-sided fractal electrode design parameters. From the results of the simulation, it could be inferred that the electrode width should be maximum for the given area on the fractal. Furthermore

the horizontal spacing between the positive and negative conductor should be minimal.

Finally, the electrode designs were tested on their plasma power capabilities. From the test results it could be seen that both the double-sided 5^{th} order Hilbert fractal and the 5^{th} order Hilbert fractal were best. By generating the most plasma either visually or mathematically. The 5^{th} order came out the best, since, due to manufacturing issues, higher order fractals were more poorly machined. However, an increase in plasma generation was observed with higher order, but out competed due to manufacturing issues. As a recommendation, it would be best to manufacture a higher order double-sided Hilbert fractal with a $0.8\,mm$ dielectric FR4 epoxy barrier.

With the testing results acquired and all plasma characteristics considered for seed disinfection in a fluidized bed, the final design choice for the plasma electrode is the double-sided 5^{th} order electrode because of the best performance regarding requirements on plasma generation on both sides, allowing for more plasma generation. However, no test were executed on the disinfection of the seeds exposed to the electrodes. Due to lack of time and testing facilities. Therefore, this should be further researched in future work, such that more specific plasma treatments can be developed.

With this work finished, a well-functioning Hilbert fractal DBD electrode in terms of plasma discharge has been designed also that fits in a fluidized bed for seed disinfection. The important mechanisms for plasma and reactive species for killing seed pathogens were investigated but not measured for the final electrode design. Therefore, for further improvements, experiments should be conducted that focus on effective disinfection cycles and ozone production rates for seeds. This could be further expanded for different kind of seeds or specific microorganisms that are common on seeds. Additionally, the effect of short-pulsed DC and duty cycle or frequency should be investigated for the designed fractal electrodes to further improve the required reactive species generation and plasma intensity. In terms of the implementation with the fluidized bed, it is recommended how the multi-hollow DBD could be further developed or better fabricated to generate plasma in the holes and act as a diffuser. In that case, the plasma can be generated from the bottom and directly lead the reactive species through the seeds.

Bibliography

[1] P. F. Lee and T. Ritmeester, “Fluidized bed with sensors for eco-friendly plasma-disinfection of seeds.”

[2] Z. Hayaty and B. Salar, “High voltage generator for eco-friendly plasma-disinfection of seeds.”

[3] M. Kim, C. Shim, J. Lee, and C. Wangchuk, “Hot water treatment as seed disinfection techniques for organic and eco-friendly environmental agricultural crop cultivation,” *Agriculture*, vol. 12, no. 8, p. 1081, Jul. 22, 2022. DOI: 10.3390/agriculture12081081. [Online]. Available: https://doi.org/10.3390/agriculture12081081.

[4] Higgins. “Hot water seed treatment.” (Nov. 2018), [Online]. Available: https://ag.umass.edu/vegetable/fact-sheets/hot-water-seed-treatment (visited on 05/28/2024).

[5] S. Singh, H. Singh, and N. K. Bharat, “Hot water seed treatment: A review,” *IntechOpen eBooks*, Mar. 3, 2020. DOI: 10.5772/intechopen.91314. [Online]. Available: https://doi.org/10.5772/intechopen.91314.

[6] N. Misra, O. Schlüter, and P. Cullen, *Plasma in food and agriculture*. Jan. 1, 2016, pp. 1–16. DOI: 10.1016/b978-0-12-801365-6.00001-9. [Online]. Available: https://doi.org/10.1016/b978-0-12-801365-6.00001-9.

[7] R. M. Kamel, M. M. El-Kholy, N. M. Tolba, A. Amer, A. M. Eltarawy, and L. M. Ali, “Influence of germicidal ultraviolet radiation uv-c on the quality of apiaceae spices seeds,” *Chemical and biological technologies in agriculture*, vol. 9, no. 1, Nov. 18, 2022. DOI: 10.1186/s40538-022-00358-4. [Online]. Available: https://doi.org/10.1186/s40538-022-00358-4.

[8] A. Waskow, A. Howling, and I. Furno, “Mechanisms of plasma-seed treatments as a potential seed processing technology,” *Frontiers in physics*, vol. 9, Apr. 14, 2021. DOI: 10.3389/fphy.2021.617345. [Online]. Available: https://doi.org/10.3389/fphy.2021.617345.

[9] R. Brandenburg, “Corrigendum: Dielectric barrier discharges: Progress on plasma sources and on the understanding of regimes and single filaments (2017 plasma sources sci. technol. 26 053001),” *Plasma sources science technology*, vol. 27, no. 7, p. 079 501, Jul. 16, 2018. DOI: 10.1088/1361-6595/aaced9. [Online]. Available: https://doi.org/10.1088/1361-6595/aaced9.

[10] M. Turner, *Physics of cold plasma*. Jan. 1, 2016, pp. 17–51. DOI: 10.1016/b978-0-12-801365-6.00002-0. [Online]. Available: https://doi.org/10.1016/b978-0-12-801365-6.00002-0.

[11] K. Liu, J. Zuo, C. Ran, *et al.*, “Reduced electric field and gas temperature effects on chemical product dynamics in air surface dielectric barrier discharges: From macro-physical parameters to micro-chemical mechanisms,” *Physical chemistry chemical physics/PCCP. Physical chemistry chemical physics*, vol. 24, no. 15, pp. 8940–8949, Jan. 1, 2022. DOI: 10.1039/d2cp00547f. [Online]. Available: https://doi.org/10.1039/d2cp00547f.

[12] D. P. Subedi, U. M. Joshi, and C. S. Wong, *Dielectric Barrier Discharge (DBD) plasmas and their applications*. Jan. 1, 2017, pp. 693–737. DOI: 10.1007/978-981-10-4217-1_13. [Online]. Available: https://doi.org/10.1007/978-981-10-4217-1_13.

[13] U. Kogelschatz, “Fundamentals and applications of dielectric-barrier discharges,” *ResearchGate*, Jan. 2000. [Online]. Available: https://www.researchgate.net/publication/228799858_Fundamentals_and_applications_of_dielectric-barrier_discharges?enrichId=rgreq-21c218eb49d1fdbbef0a3bf1c9ba73d8-XXX&enrichSource=Y292ZXJQYWdlOzIyODc5OTg1ODtBU1_x_2&_esc=publicationCoverPdf.

[14] K. Tanaka, *Plasma thermal and nonthermal technologies*. Jan. 1, 2022, pp. 13–24. DOI: 10.1007/978-981-16-3891-6_2. [Online]. Available: https://doi.org/10.1007/978-981-16-3891-6_2.

[15] P. Lu, P. Cullen, and K. Ostrikov, *Atmospheric pressure nonthermal plasma sources*. Jan. 1, 2016, pp. 83–116. DOI: 10.1016/b978-0-12-801365-6.00004-4. [Online]. Available: https://doi.org/10.1016/b978-0-12-801365-6.00004-4.

[16] J. M. Williamson, D. D. Trump, P. Bletzinger, and B. N. Ganguly, “Comparison of high-voltage ac and pulsed operation of a surface dielectric barrier discharge,” *Journal of physics. D, Applied physics*, vol. 39, no. 20, pp. 4400–4406, Sep. 29, 2006. DOI: 10.1088/0022-3727/39/20/016. [Online]. Available: https://doi.org/10.1088/0022-3727/39/20/016.

[17] H. Jiang and T. Shao, *Surface dielectric barrier discharge driven by nanosecond pulses*. Springer, Jan. 1, 2023, pp. 635–672. DOI: 10.1007/978-981-99-1141-7_23. [Online]. Available: https://doi.org/10.1007/978-981-99-1141-7_23.

[18] N. D. Wilde, H. Xu, N. Gomez-Vega, and S. R. H. Barrett, "A model of surface dielectric barrier discharge power," *Applied physics letters*, vol. 118, no. 15, Apr. 12, 2021. DOI: 10.1063/5.0043339. [Online]. Available: https://doi.org/10.1063/5.0043339.

[19] S. Patil, P. Bourke, and P. Cullen, *Principles of nonthermal plasma decontamination*. Jan. 1, 2016, pp. 143–177. DOI: 10.1016/b978-0-12-801365-6.00006-8. [Online]. Available: https://doi.org/10.1016/b978-0-12-801365-6.00006-8.

[20] F. Avino, A. A. Howling, M. Von Allmen, *et al.*, "Surface dbd degradation in humid air, and a hybrid surface-volume dbd for robust plasma operation at high humidity," *Journal of physics. D, Applied physics*, vol. 56, no. 34, p. 345 201, May 18, 2023. DOI: 10.1088/1361-6463/acd2e4. [Online]. Available: https://doi.org/10.1088/1361-6463/acd2e4.

[21] J. Mravlje, M. Regvar, P. Starič, M. Mozetič, and K. Vogel-Mikuš, "Cold plasma affects germination and fungal community structure of buckwheat seeds," *Plants*, vol. 10, no. 5, p. 851, Apr. 23, 2021. DOI: 10.3390/plants10050851. [Online]. Available: https://doi.org/10.3390/plants10050851.

[22] J. Mravlje, M. Regvar, and K. Vogel-Mikuš, "Development of cold plasma technologies for surface decontamination of seed fungal pathogens: Present status and perspectives," *Journal of Fungi*, vol. 7, no. 8, p. 650, Aug. 11, 2021. DOI: 10.3390/jof7080650. [Online]. Available: https://doi.org/10.3390/jof7080650.

[23] A. Zahoranová, L. Hoppanová, J. Šimončicová, *et al.*, "Effect of cold atmospheric pressure plasma on maize seeds: Enhancement of seedlings growth and surface microorganisms inactivation," *Plasma chemistry and plasma processing*, vol. 38, no. 5, pp. 969–988, Jun. 9, 2018. DOI: 10.1007/s11090-018-9913-3. [Online]. Available: https://doi.org/10.1007/s11090-018-9913-3.

[24] T. Nishioka, Y. Takai, M. Kawaradani, *et al.*, "Seed disinfection effect of atmospheric pressure plasma and low pressure plasma on rhizoctonia solani," *Biocontrol science*, vol. 19, no. 2, pp. 99–102, Jan. 1, 2014. DOI: 10.4265/bio.19.99. [Online]. Available: https://doi.org/10.4265/bio.19.99.

[25] Y. Jo, J. Cho, T. Tsai, *et al.*, "A non□thermal plasma seed treatment method for management of a seedborne fungal pathogen on rice seed," *Crop science*, vol. 54, no. 2, pp. 796–803, Mar. 1, 2014. DOI: 10.2135/cropsci2013.05.0331. [Online]. Available: https://doi.org/10.2135/cropsci2013.05.0331.

[26] S. Das, V. P. Gajula, S. Mohapatra, G. Singh, and S. Kar, "Role of cold atmospheric plasma in microbial inactivation and the factors affecting its efficacy," *Health sciences review*, vol. 4, p. 100 037, Sep. 1, 2022. DOI: 10.1016/j.hsr.2022.100037. [Online]. Available: https://doi.org/10.1016/j.hsr.2022.100037.

[27] Y. Meng, G. Qu, T. Wang, Q. Sun, D. Liang, and S. Hu, "Enhancement of germination and seedling growth of wheat seed using dielectric barrier discharge plasma with various gas sources," *Plasma chemistry and plasma processing*, vol. 37, no. 4, pp. 1105–1119, Feb. 17, 2017. DOI: 10.1007/s11090-017-9799-5. [Online]. Available: https://doi.org/10.1007/s11090-017-9799-5.

[28] S. Yu, W. Wang, Q. Jiang, L. Hu, and J. He, "Breakdown characteristics of epoxy dielectric film under high frequency square wave voltage," *2022 IEEE 4th International Conference on Dielectrics (ICD)*, Jul. 2022. DOI: 10.1109/icd53806.2022.9863557. [Online]. Available: https://doi.org/10.1109/icd53806.2022.9863557.

[29] W. Zhao, T. Luo, and M. G. Niasar, "Ramp sinusoidal breakdown of epoxy resin under high voltage waveforms at different frequencies," *TU Delft Institutional Repository*, Jan. 2021. DOI: 10.1049/icp.2022.0291. [Online]. Available: https://doi.org/10.1049/icp.2022.0291.

[30] S. Grzybowski, E. Feilat, P. Knight, and L. Doriott, "Breakdown voltage behavior of PET thermoplastics at DC and AC voltages," *Reseachgate.net*, Jan. 2003. DOI: 10.1109/secon.1999.766141. [Online]. Available: https://doi.org/10.1109/secon.1999.766141.

[31] A. A. Garamoon, D. M. El-Zeer, A. A. E. Ghany, D. Ghoneem, and F. El-Hossary, "Influences of the barrier types and arrangements on dielectric barrier discharge characteristics," *EPJ. Applied physics/□The □European physical journal. Applied physics*, vol. 53, no. 2, p. 21 001, Jan. 2011. DOI: 10.1051/epjap/2010100196. [Online]. Available: https://www.cambridge.org/core/journals/the-european-physical-journal-applied-physics/article/influences-of-the-barrier-types-and-arrangements-on-dielectric-barrier-discharge-characteristics/076E222120332ED2E980D3B60C77C00C.

[32] J. Jablons. “Top applications for gold-plated tungsten wire - metal cutting corporation.” (May 14, 2020), [Online]. Available: https://metalcutting.com/knowledge-center/top-applications-for-gold-plated-tungsten-wire/ (visited on 06/13/2024).

[33] T. Homola, R. Krumpolec, M. Zemánek, *et al.*, “An array of micro-hollow surface dielectric barrier discharges for large-area atmospheric-pressure surface treatments,” *Plasma chemistry and plasma processing*, vol. 37, no. 4, pp. 1149–1163, Feb. 21, 2017. DOI: 10.1007/s11090-017-9792-z. [Online]. Available: https://doi.org/10.1007/s11090-017-9792-z.

[34] R. Krumpolec, V. Richter, M. Zemánek, and T. Homola, “Multi-hollow surface dielectric barrier discharge for plasma treatment of patterned silicon surfaces,” *Surfaces and interfaces*, vol. 16, pp. 181–187, Sep. 1, 2019. DOI: 10.1016/j.surfin.2019.01.014. [Online]. Available: https://doi.org/10.1016/j.surfin.2019.01.014.

[35] R. Cimerman, E. Maťaš, M. Sárený, and K. Hensel, “Electrical and optical characterization of multi-hollow surface dielectric barrier discharge in configuration with the air-exposed electrode,” *Physics of plasmas*, vol. 29, no. 11, Nov. 1, 2022. DOI: 10.1063/5.0101496. [Online]. Available: https://doi.org/10.1063/5.0101496.

[36] Y. Zhao, Y. Shi, S. Liu, *et al.*, “Study on the mode transition of multi-hollow dielectric barrier discharge,” *Journal of applied physics*, vol. 134, no. 10, Sep. 8, 2023. DOI: 10.1063/5.0151610. [Online]. Available: https://doi.org/10.1063/5.0151610.

[37] CIF, “Cif 090917, Copper-cladded epoxy base prototyping board,” Nov. 13, 2008, pp. 1–6. [Online]. Available: https://www.farnell.com/datasheets/87452.pdf (visited on 05/20/2024).

[38] P. Warlitz, M. T. Hehner, S. Pasch, J. Serpieri, T. Blank, and J. Kriegseis, “On durable materials for dielectric-barrier discharge plasma actuators,” *Sensors and actuators. A, Physical*, vol. 366, p. 114 985, Feb. 2024. DOI: 10.1016/j.sna.2023.114985. [Online]. Available: https://doi.org/10.1016/j.sna.2023.114985.

[39] M. Bader, H. Bungartz, and M. Mehl, *Space-Filling curves*. Springer Ebooks, Jan. 1, 2011, pp. 1862–1867. DOI: 10.1007/978-0-387-09766-4_145. [Online]. Available: https://doi.org/10.1007/978-0-387-09766-4_145.

[40] P. Anagha, S. G. G. S, and N. Abraham, “Simulation studies on the design and analysis of interdigital and fractal-based micro-supercapacitors,” *ECS journal of solid state science and technology*, vol. 12, no. 6, p. 061 003, Jun. 1, 2023. DOI: 10.1149/2162-8777/acdd99. [Online]. Available: https://doi.org/10.1149/2162-8777/acdd99.

[41] U. Kogelschatz, “Collective phenomena in volume and surface barrier discharges,” *Journal of physics. Conference series*, vol. 257, p. 012 015, Nov. 1, 2010. DOI: 10.1088/1742-6596/257/1/012015. [Online]. Available: https://doi.org/10.1088/1742-6596/257/1/012015.

[42] E. Engineeringtoolbox, *Relative Permittivity - the Dielectric Constant*, Feb. 2024. [Online]. Available: https://www.engineeringtoolbox.com/relative-permittivity-d_1660.html.

[43] J. Kim, S. Park, and W. Choe, “Surface plasma with an inkjet-printed patterned electrode for low-temperature applications,” *Scientific reports*, vol. 11, no. 1, Jun. 9, 2021. DOI: 10.1038/s41598-021-91720-3. [Online]. Available: https://doi.org/10.1038/s41598-021-91720-3.

[44] COMSOL BV, *Comsol multiphysics*, comp. software, version 6.2. [Online]. Available: https://www.comsol.com/products.

[45] OpenStax. “8.3: Capacitors in series and in parallel.” (Sep. 12, 2022), [Online]. Available: https://phys.libretexts.org/Bookshelves/University_Physics/University_Physics_%28OpenStax%29/Book%3A_University_Physics_II_-_Thermodynamics_Electricity_and_Magnetism_%28OpenStax%29/08%3A_Capacitance/8.03%3A_Capacitors_in_Series_and_in_Parallel (visited on 06/14/2024).

[46] H. Jiang Jr., T. Shao, C. Zhang, *et al.*, “Experimental Study of Q-V Lissajous Figures in Nanosecond-Pulse Surface Discharges,” Tech. Rep. 4, Aug. 2013, pp. 1101–1102.

[47] *Numpy.Trapz — NumPy V1.26 Manual*. [Online]. Available: https://numpy.org/doc/stable/reference/generated/numpy.trapz.html.

A

Appendix A

Appendix A contains all the pictures taken from the elctrodes

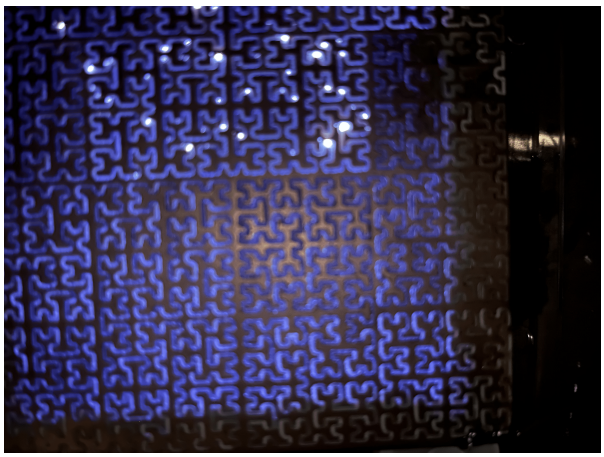

Figure A.1: 6th order fully on (more).png

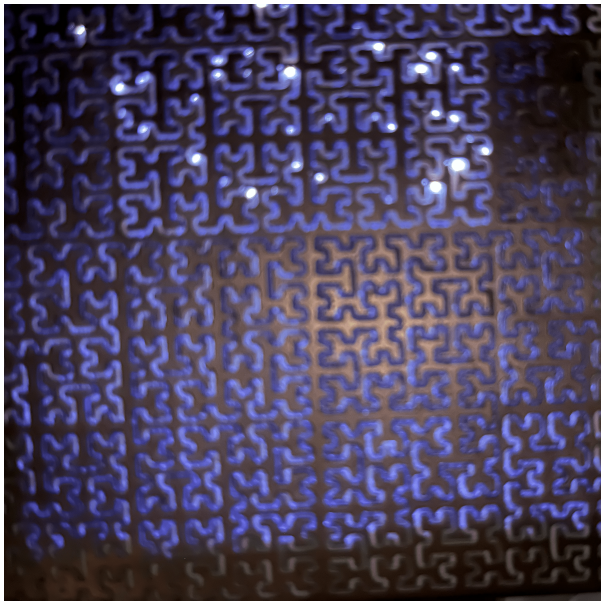

Figure A.2: 6th order fully on.png

Figure A.3: 6th order hilbert turn on.png

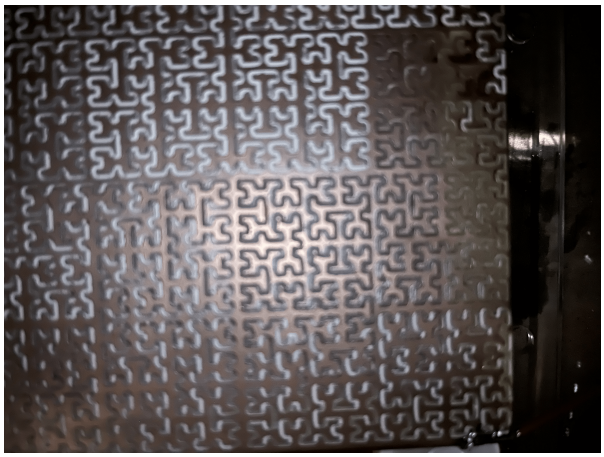

Figure A.4: 6th order hilbr off.png

Figure A.5: Coplanar.png

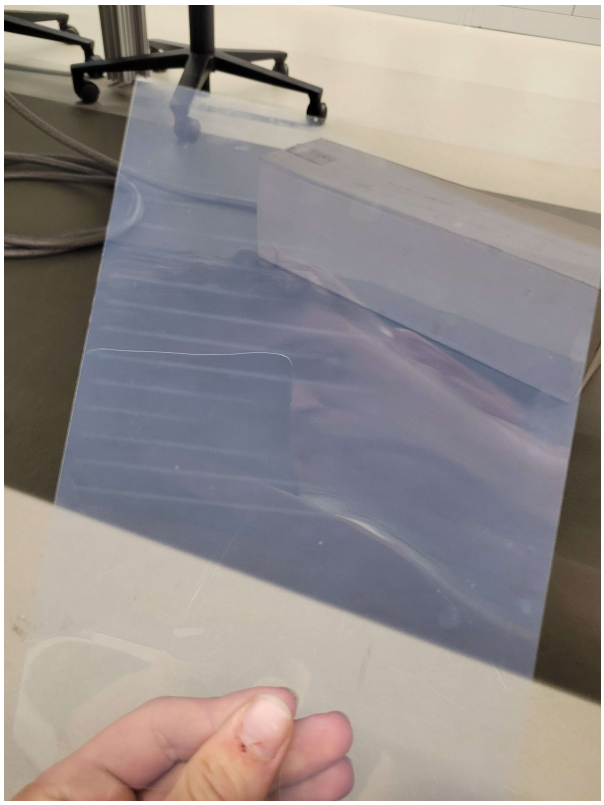

Figure A.6: Damage DBD.jpg

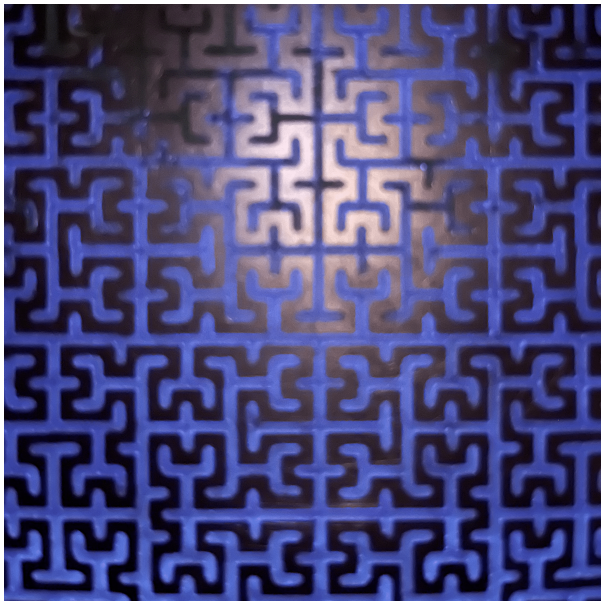

Figure A.7: Double Sided back (fully).png

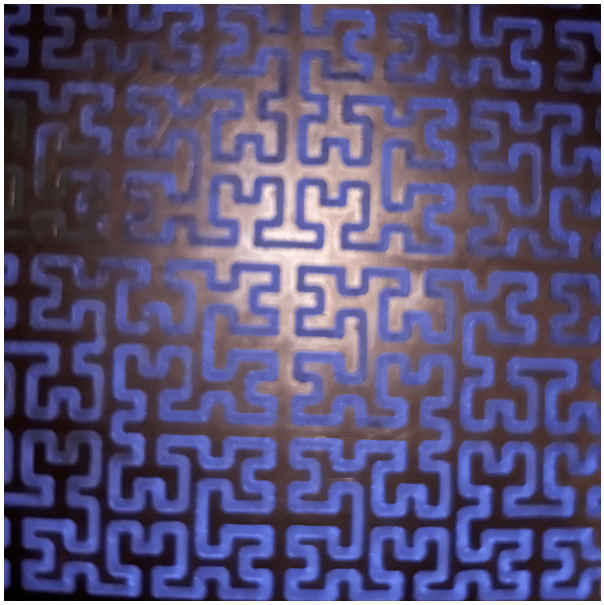

Figure A.8: Double Sided front (fully).png

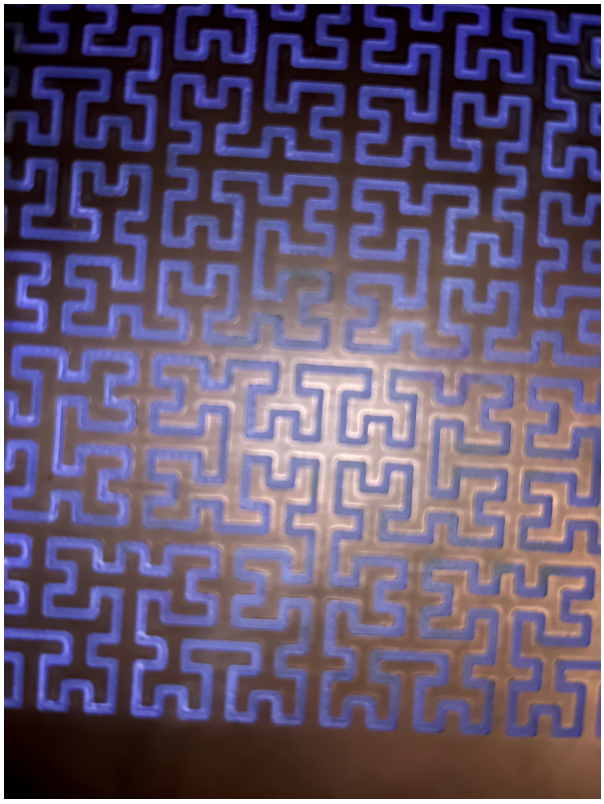

Figure A.9: Hilber 1.6 mm (on).jpg

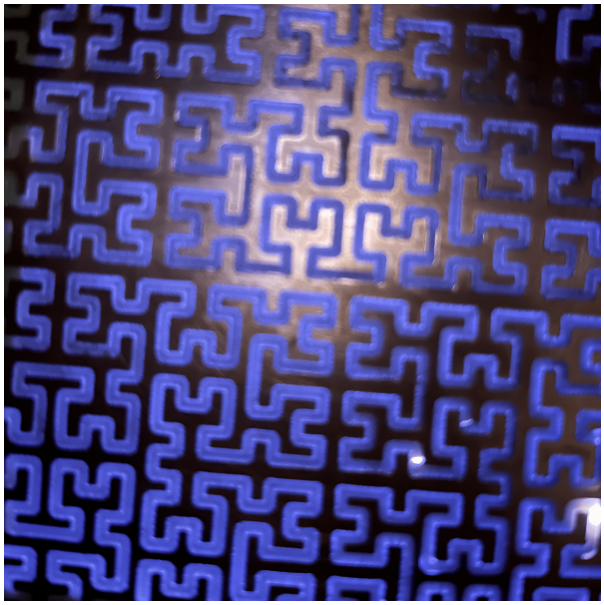

Figure A.10: Hilbert 5th 0.8mm fully on.png

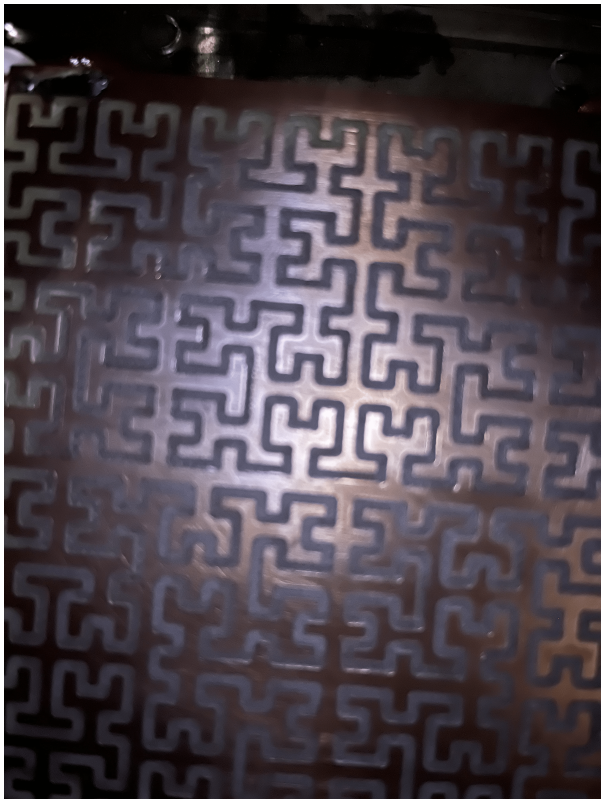

Figure A.11: Hilbert 5th 0.8mm off.png

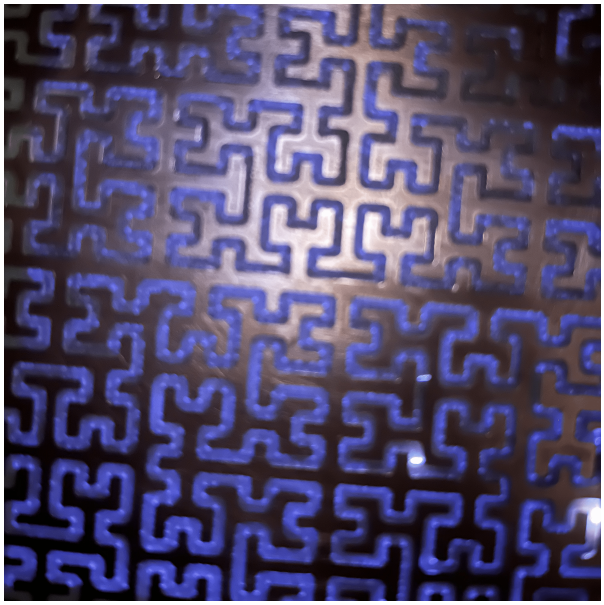

Figure A.12: Hilbert 5th 0.8mm partially on.png

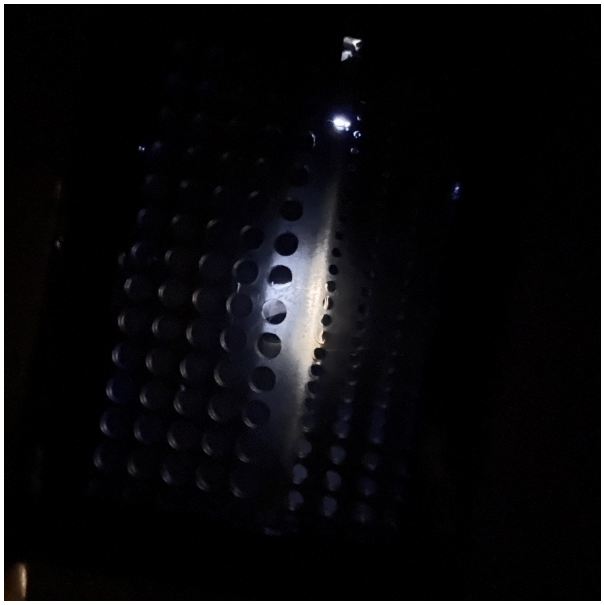

Figure A.13: Hollow sheet turning on 2.png

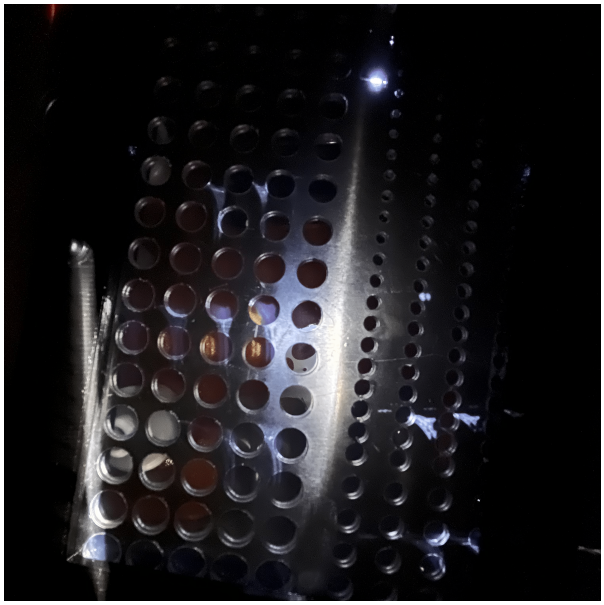

Figure A.14: Hollow sheet turning on.png

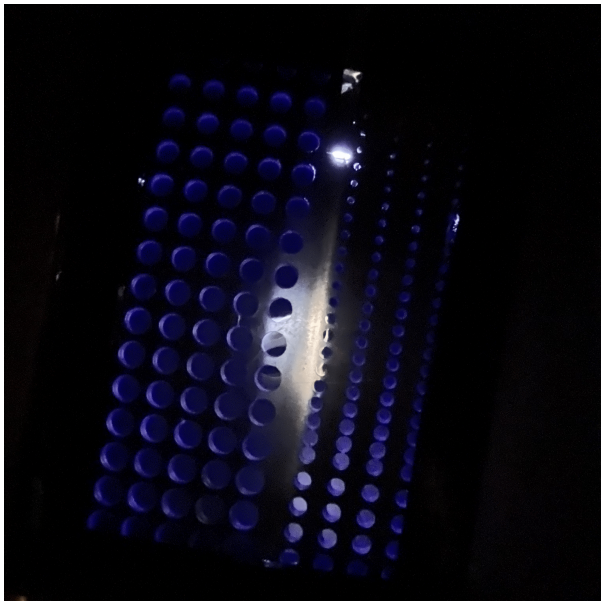

Figure A.15: Hollowsheet fully on.png

Figure A.16: Peano (off).jpg

Figure A.17: Peano (on).jpg

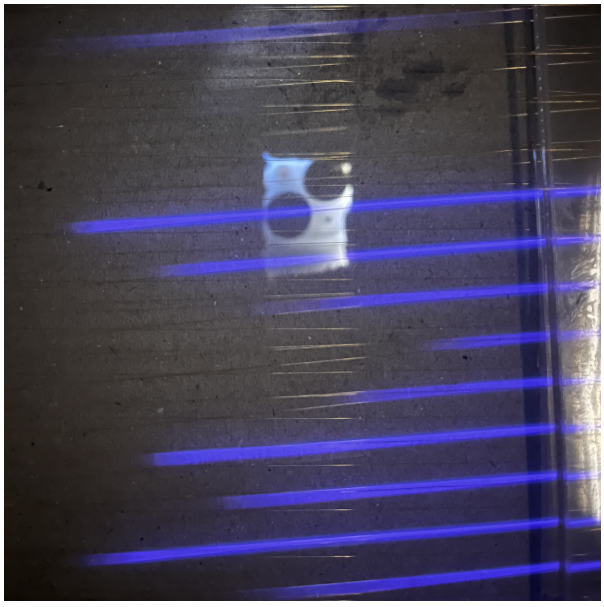

Figure A.18: Wire - sheet partially on.jpeg

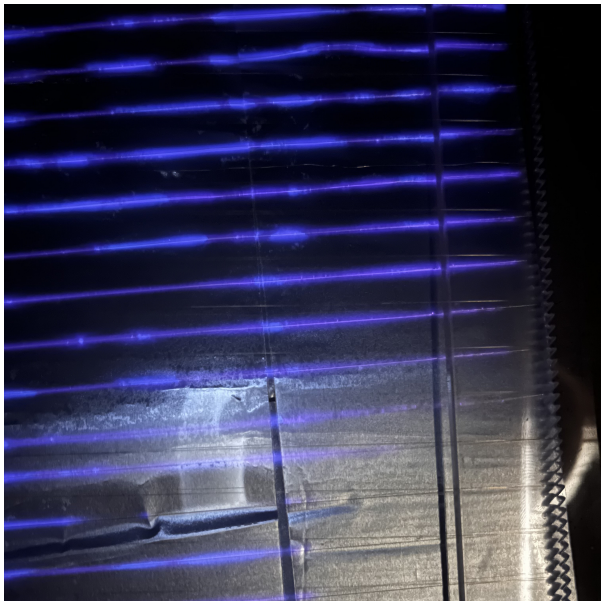

Figure A.19: Wire to sheet fully on (more).jpeg

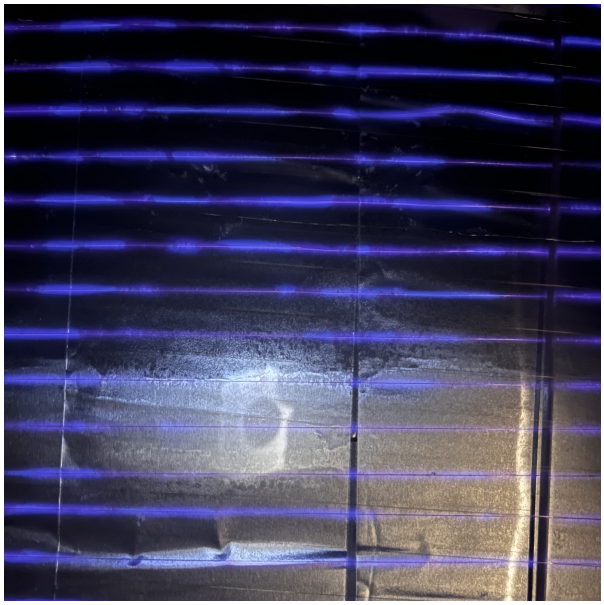

Figure A.20: wire to sheet fully on.jpeg

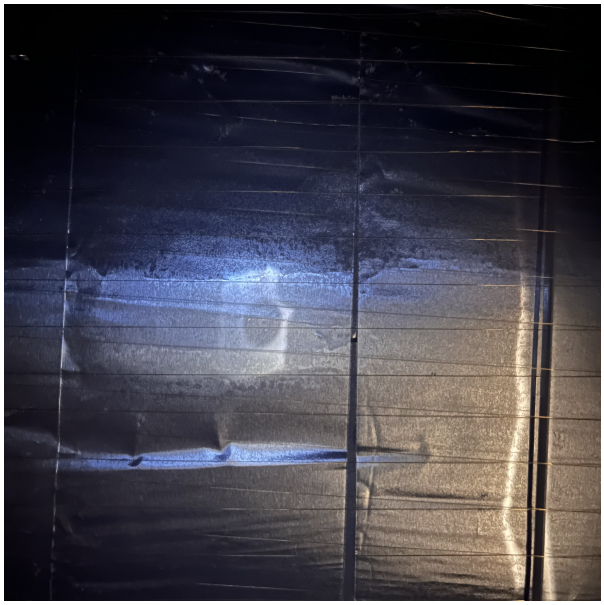

Figure A.21: wire to sheet off.jpeg

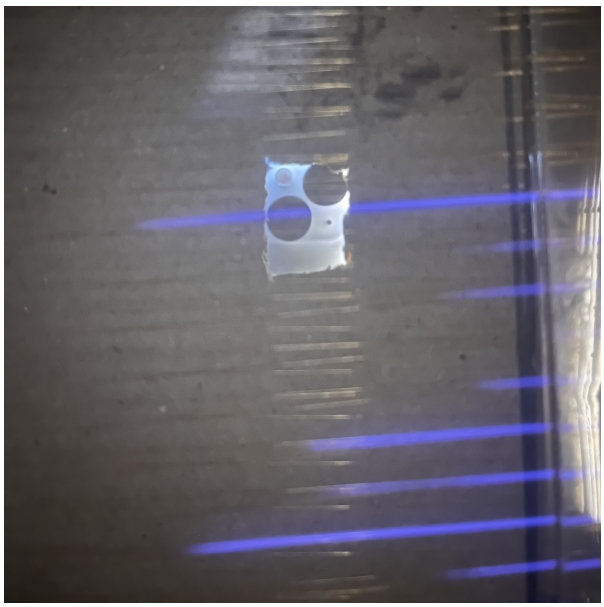

Figure A.22: Wire to Wire.jpeg

B

Appendix B

Appendix B contains all the python plots

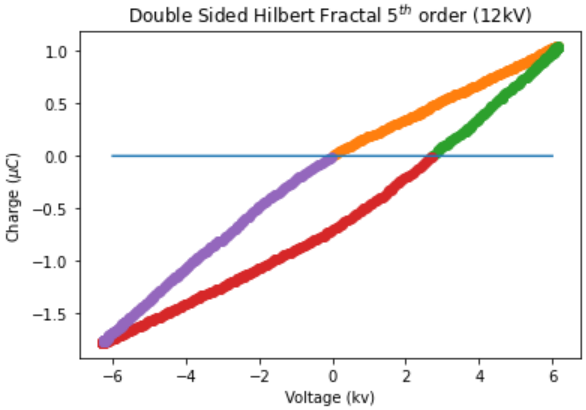

Figure B.1: Debug.png

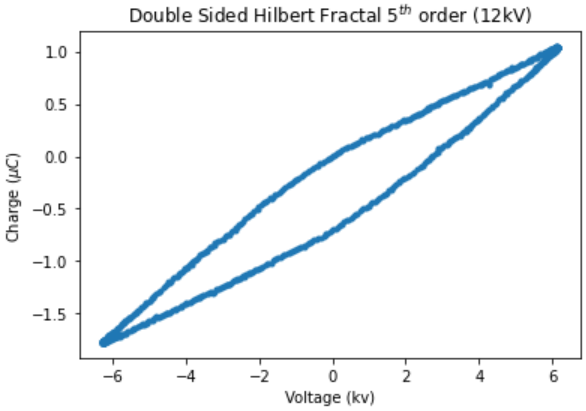

Figure B.2: Double$_sided.png$

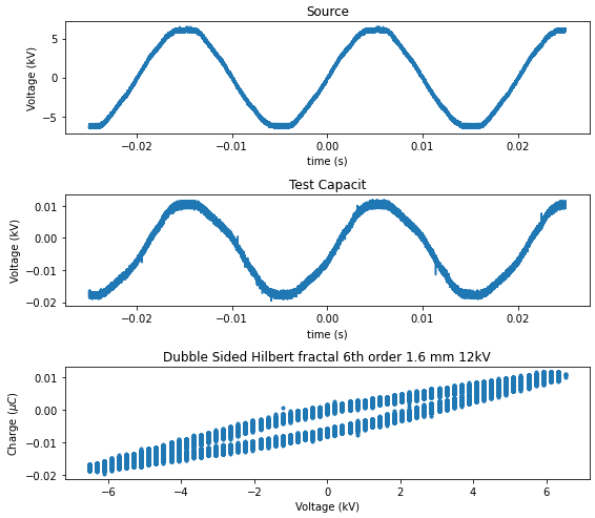

Figure B.3: Double$_sided_full(unfiltered).png$

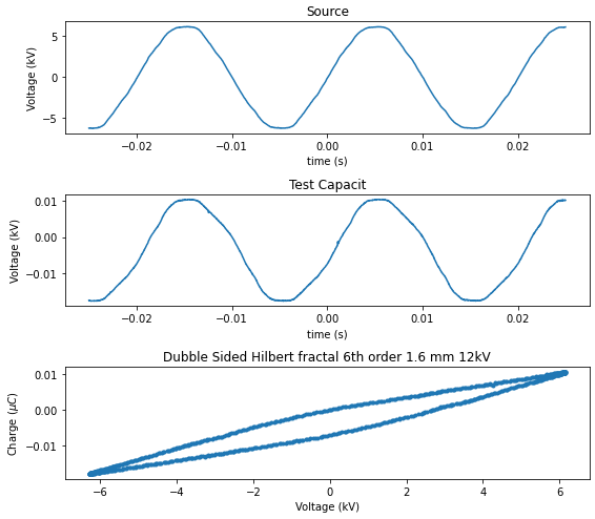

Figure B.4: Double$_sided_full.png$

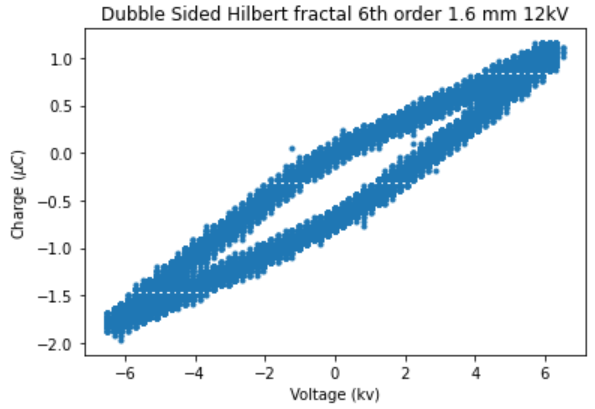

Figure B.5: Dubble Sided 12kV (unfiltered).png

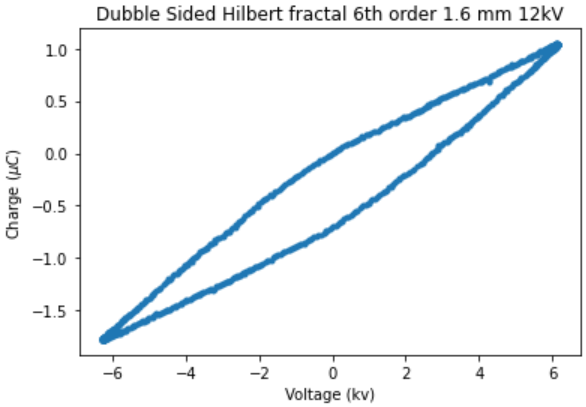

Figure B.6: Dubble Sided 12kV.png

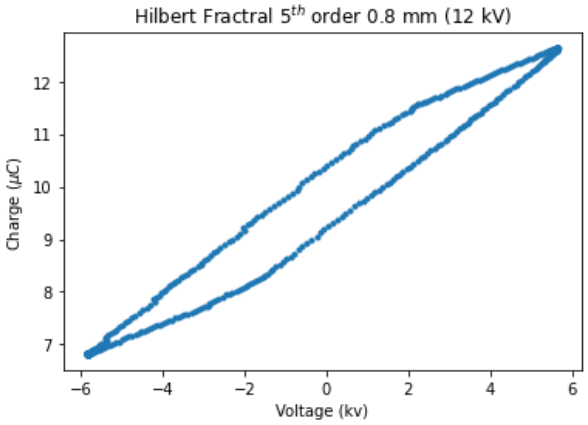

Figure B.7: Hilbert 5th 08mm 12kV.png

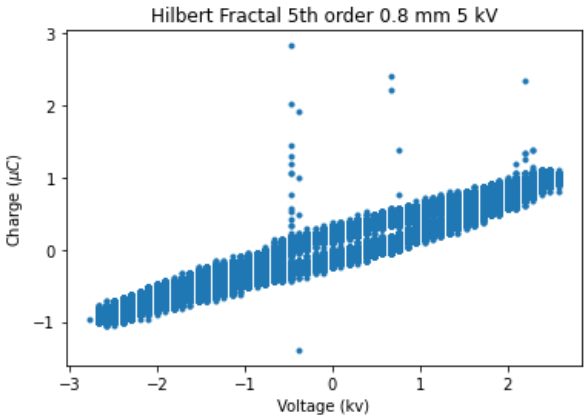

Figure B.8: Hilbert 5th 08mm 5kV (unfiltered).png

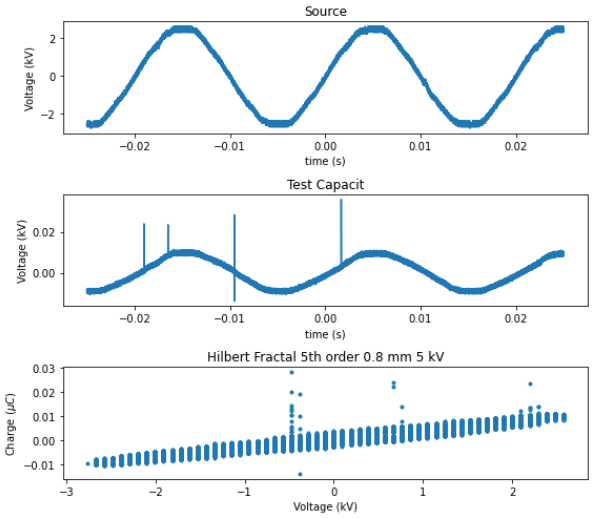

Figure B.9: Hilbert 5th 08mm 5kV full (unfiltered).png

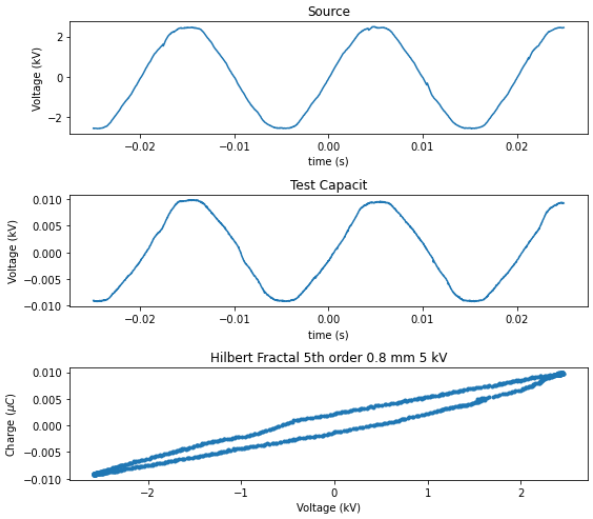

Figure B.10: Hilbert 5th 08mm 5kV full.png

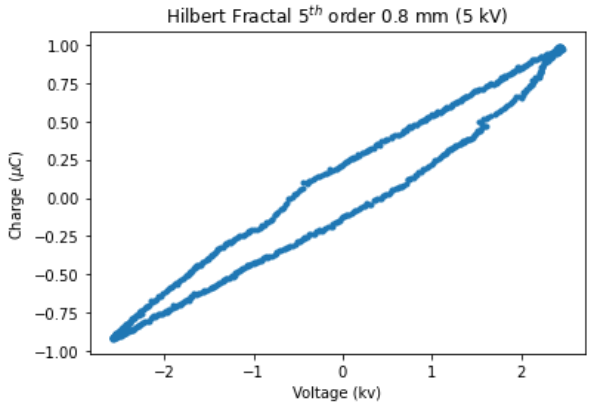

Figure B.11: Hilbert 5th 08mm 5kV.png

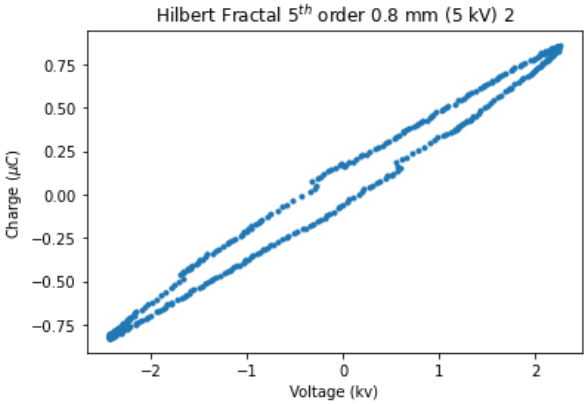

Figure B.12: Hilbert 5th 08mm 5kV$_2$.png

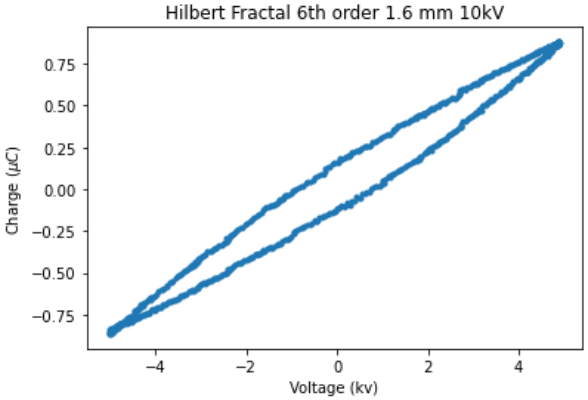

Figure B.13: Hilbert 5th 16mm 10kV.png

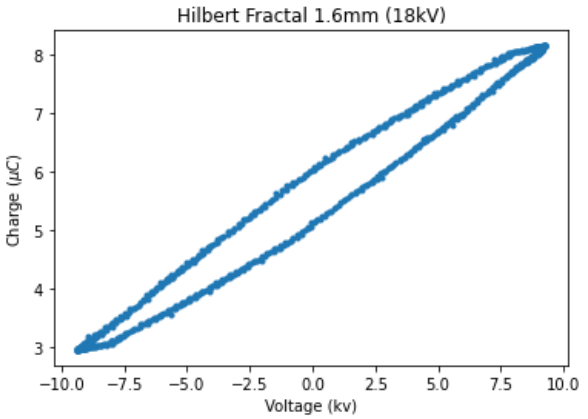

Figure B.14: Hilbert 5th 16mm 18kV.png

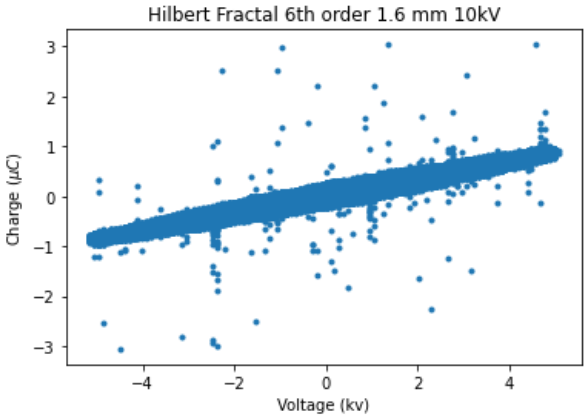

Figure B.15: Hilbert 6th 16mm 10kV (unfiltered).png

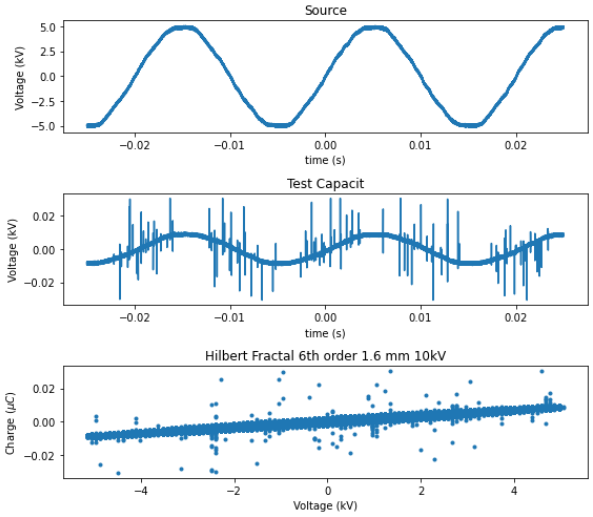

Figure B.16: Hilbert 6th 16mm 10kV full (unfiltered).png

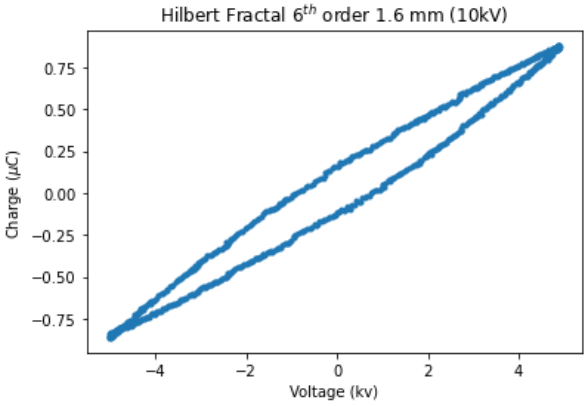

Figure B.17: Hilbert 6th 16mm 10kV full.png

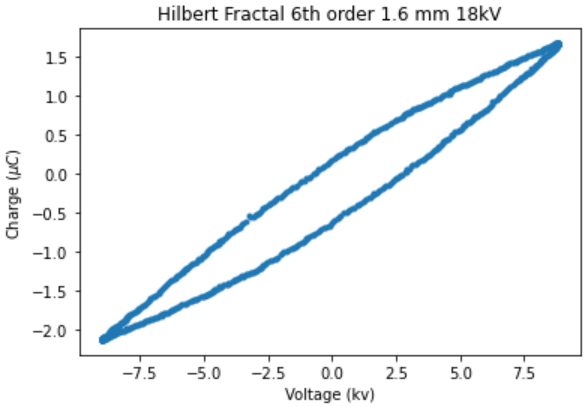

Figure B.18: Hilbert 6th 18kV.png

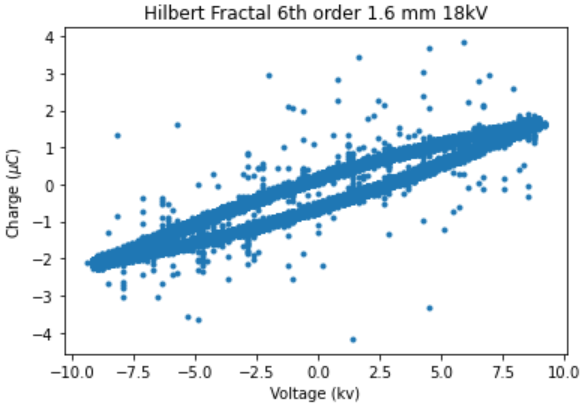

Figure B.19: Hilbert 6th order 18kV (unfiltered).png

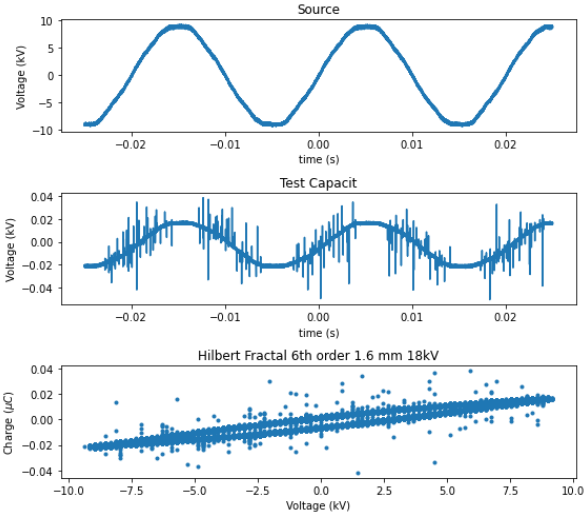

Figure B.20: Hilbert 6th order 18kV full (unfiltered).png

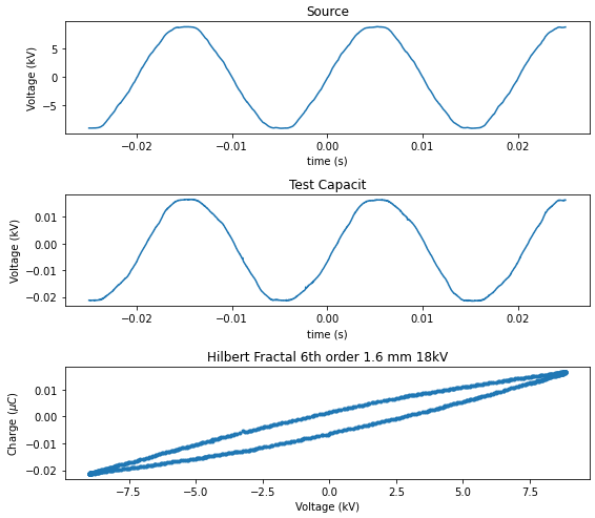

Figure B.21: Hilbert 6th order 18kV full.png

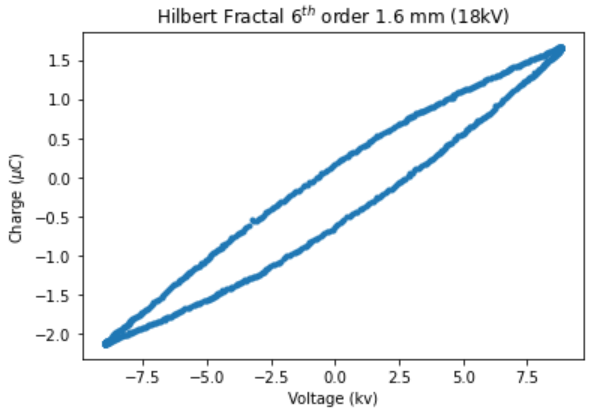

Figure B.22: Hilbert 6th order 18kV.png

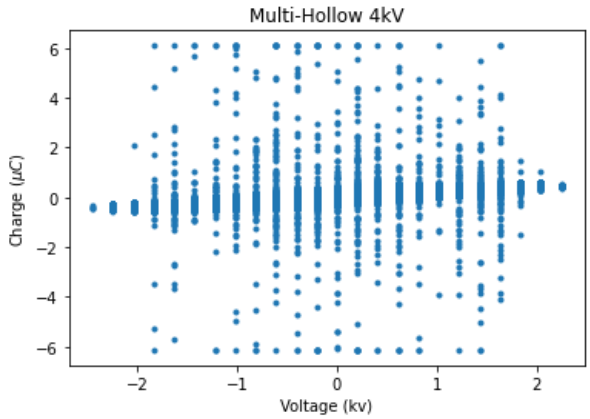

Figure B.23: Multi-Hollow 4kV (unfiltered).png

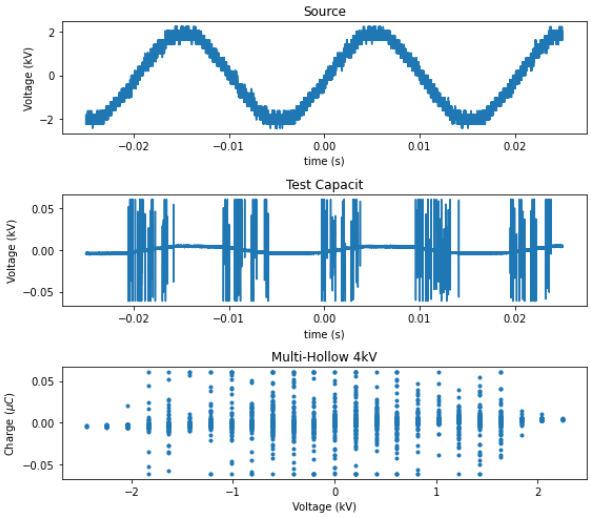

Figure B.24: Multi-Hollow 4kV full (unfiltered).png

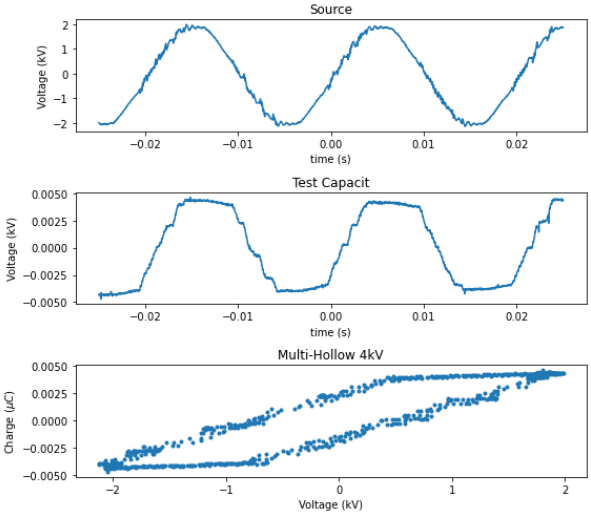

Figure B.25: Multi-Hollow 4kV full.png

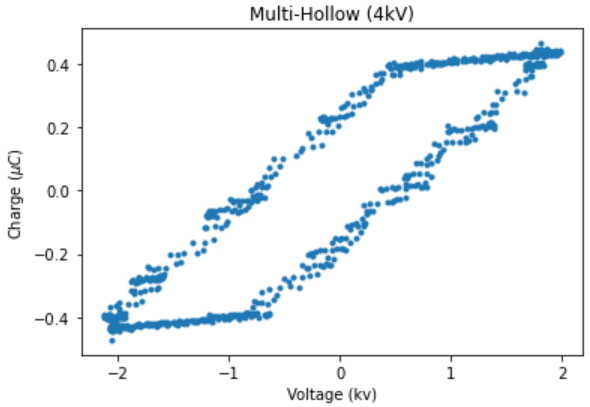

Figure B.26: Multi-Hollow 4kV.png

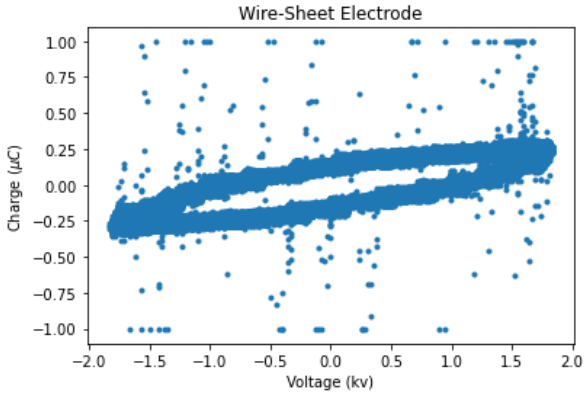

Figure B.27: Wire-Sheet Electrode (unflitered).png

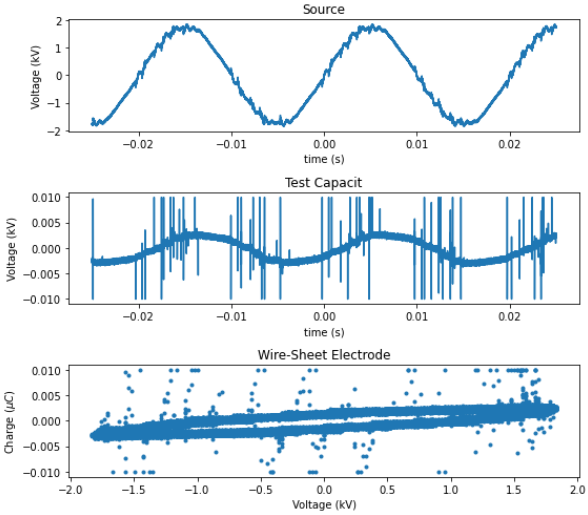

Figure B.28: Wire-Sheet Electrode full (unflitered).png

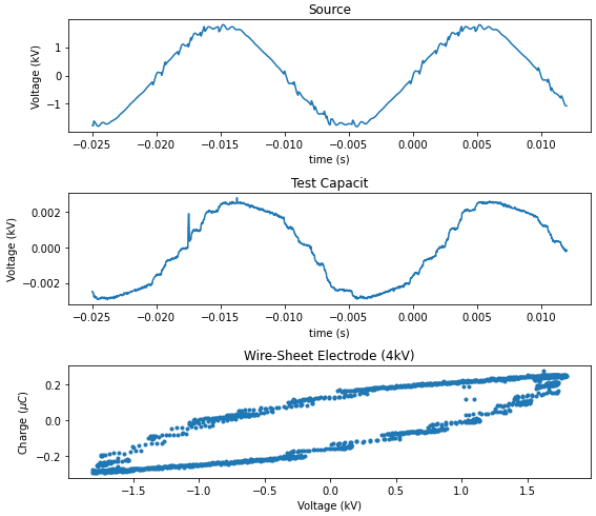

Figure B.29: Wire-Sheet Electrode full.png

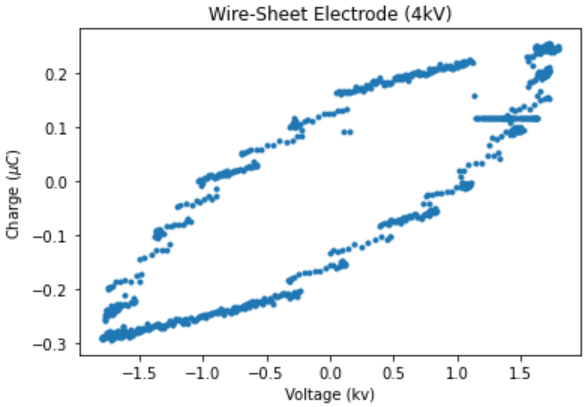

Figure B.30: Wire-Sheet Electrode.png

Appendix C

Appendix C shows all the used python code in this research

```
# -*- coding: utf-8 -*-
"""
Spyder Editor

This is a temporary script file.
"""

import numpy as np
import matplotlib.pyplot as plt
import matplotlib.gridspec as gridspec
import pandas as pd
import glob

#Filter Data
def smoothen(y, tolerance):
    for n in range(1,len(y)-1):
        if y[n-1] - y[n] < tolerance:
            if y[n-1] - y[n] > -tolerance:
                continue
            else:
                y[n] = y[n-1]
        else:
            y[n] = y[n-1]
    return y

def integrate(array, step):
    # Reshape the array into a 2D array with 5 rows
    data_2d = np.reshape(array, (-1, step))

    # Calculate the average of each row
    averages = np.mean(data_2d, axis=1)

    # Convert the averages back into a 1D array
    averaged_data = averages.flatten()
    return averaged_data

def filtering(y):
    # Calculate the 25th and 75th percentiles
    q25 = np.percentile(y, 40)
    q75 = np.percentile(y, 60)

    # Calculate the interquartile range (IQR)
    iqr = q75 - q25

    # Filter out data points with values outside the IQR
    filtered_data = [x for x in y if q25 - 1.5 * iqr <= x <= q75 + 1.5 * iqr]
    return filtered_data

# specify the directory path
directory = 'Data'

# get a list of files in the directory
files = glob.glob(directory + '/*')
```

```
# print the file names
for file in files:
    # Load the CSV file
    df = pd.read_csv(file)

    # Extract the x and y columns
    x = df['CH1(V)'].values
    y = df['CH2(V)'].values
    #y=y-9/(1000*100e-3)
    t = df['Time(s)'].values



    # for i in range(0,5):
    #     y = smoothen(y,0.1)


    start = int(len(t)*0.01/0.1)
    start =  int(np.where(x[:start] ==np.min(x[:start]))[0][0])
    stop = int(1e5-start)

    x = x[start:-stop]
    y = y[start:-stop]
    t = t[start:-stop]


    # stop = int(len(t)*0.037/0.05)

    # x = x[:stop]
    # y = y[:stop]
    # t = t[:stop]
    x = integrate(x,500)
    y = integrate(y,500)
    t = integrate(t, 500)


    # y = smoothen(y, 0.1)
    #y = filtering(y)

    singlecircle = int(len(t)*0.02/(t[-1]-t[0]))



    # # Create a figure and axis
    # fig = plt.figure(figsize=(8, 7))
    # gs = gridspec.GridSpec(3, 1)

    # # Create two subplots
    # ax1 = fig.add_subplot(gs[0])
    # ax2 = fig.add_subplot(gs[1])
    # ax3 = fig.add_subplot(gs[2])
    # # Plot on each subplot
    # ax1.plot(t, x)
    # ax1.set_title('Source')
    # ax1.set_xlabel('time (s)')
    # ax1.set_ylabel('Voltage (kV)')

    # ax2.plot(t[:len(y)], y)
    # ax2.set_title('Test Capacit')
    # ax2.set_xlabel('time (s)')
    # ax2.set_ylabel('Voltage (kV)')
    # #ax2.set_xlim(-0.0190170001, -0.0190169999)



    # ax3.scatter(x[:singlecircle],1000*100e-9*1e6*y[:singlecircle], marker = '.')
    # ax3.set_title(file[5:-4])
    # ax3.set_xlabel('Voltage (kV)')
    # ax3.set_ylabel('Charge ($\mu C$)')

    y_larger_0 = np.compress(y[:singlecircle]>=0, y[:singlecircle])
    y_smaller_0 = np.compress(y[:singlecircle]<0, y[:singlecircle])
```

```
half = int(np.where(x[:singlecircle] ==np.max(x[:singlecircle]))[0][0])
skip = int(len(np.compress(y[:half]<0, y[:half])))

#area = np.trapz(y[half:2*half]*1000*100e-9, x[hlaf:2*half]*1000)

uppercurve =np.trapz(1000*100e-9*np.flip(y[half:len(y_larger_0)+skip]),
 ↪  1000*np.flip(x[half:len(y_larger_0)+skip]))-np.trapz(1000*100e-9*y[skip:half],
 ↪  1000*x[skip:half])
lowercurve = np.trapz(1000*100e-9*np.flip(y[:skip]),1000*np.flip(x[:skip])) -
 ↪  np.trapz(1000*100e-9*y[skip+len(y_larger_0):singlecircle],
 ↪  1000*x[skip+len(y_larger_0):singlecircle])
area = uppercurve+lowercurve

#ax3.fill_between(x, y, alpha=0.3)
# ax3.set_xlabel('Voltage (kV)')
# ax3.set_ylabel('Charge ($\mu C$)')
# ax3.set_title(file[5:-4])
# #ax3.text(0.5, 0.5, f'Area: {area:.2f}', ha='center', va='center')
# fig.tight_layout()
# plt.show()


# plt.scatter(x[:singlecircle],1000*100e-9*1e6*y[:singlecircle], marker='.')


# plt.scatter( np.flip(x[half:len(y_larger_0)+skip]),
 ↪  1e6*1000*100e-9*np.flip(y[half:len(y_larger_0)+skip]))
# plt.scatter((x[skip:half]),1000*100e-3*(y[skip:half]))

# plt.scatter(x[:skip],1000*100e-3*y[:skip])
# plt.scatter(x[skip+len(y_larger_0):singlecircle],
 ↪  1000*100e-3*y[skip+len(y_larger_0):singlecircle])

# xi = np.arange(int(min(x)),int(max(x)), 0.001)
# yi = np.zeros(len(xi))
# plt.plot(xi,yi)


plt.title(file[5:-4])
plt.ylabel('Charge ($\mu C$)')
plt.xlabel('Voltage (kv)')
# Show the plot
plt.show()

V_source = (max(x)-min(x))*1000
V_test = (max(y)-min(y))*1000
Q =  V_test*100e-9

print('-----------------------------------')
print(file[5:])
print("Supply Voltage: ", V_source/1000, 'kV')
print("Charge Capacitor: ",Q, 'C')
print("The power is: ", 50*area, 'W')
print('-----------------------------------')
```

Python code for plotting Lissajous

```
# -*- coding: utf-8 -*-
"""
Created on Fri Jun 14 12:26:15 2024

@author: SID-DRW
"""

import os

dir_path = 'Pictures'
file_list = [f for f in os.listdir(dir_path) if os.path.isfile(os.path.join(dir_path, f))]

name  = '\def\names{'
for file in file_list[:-1]:
    name = name + '{Figures/Pictures Electrodes/' + file + '}, '

name = name + '{Figures/Pictures Electrodes/' + file_list[-1] + '}}'
print(repr(name))
```

Part of the code to auto generate figures in the appendix